Universität Hamburg
DER FORSCHUNG | DER LEHRE | DER BILDUNG

FAKULTÄT
FÜR MATHEMATIK, INFORMATIK
UND NATURWISSENSCHAFTEN

Master's Thesis

Spectral Climate Feedback Parameter in Models and Observations

Florian Römer

florian.roemer@studium.uni-hamburg.de
Course: M.Sc. Meteorology
Matr.-No. 6937660

Primary supervisor: Prof. Dr. Stefan Bühler
Secondary supervisor: Dr. Manfred Brath

Submission: 19 August 2021

Abstract

The climate feedback parameter (λ) indicates how sensitive Earth's radiation balance responds to temperature changes. To investigate the mechanisms by which different climate feedbacks operate, I extend the analysis from the broadband λ to the spectral feedback parameter λ_ν, which I infer from hyperspectral satellite observations of outgoing radiances provided by the Infrared Atmospheric Sounding Interferometer (IASI). Similarly, I simulate observations for three different climate models participating in the Coupled Model Intercomparison Project Phase 6 (CMIP6), additionally including the far-infrared (FIR). For this approach, I regress interannual variations of the clear-sky spectral outgoing longwave radiation over the tropical ocean against the atmospheric temperature at 500 hPa.

The broadband λ inferred are consistent with values from other studies. The resulting λ_ν differ substantially between the IASI observations and the models and also between the models themselves. While the observations agree very well with most of the models in the water vapour (H_2O) absorption band in the mid-infrared (MIR), they show more negative and hence more stable values for λ_ν in the atmospheric window (AW).

A feedback decomposition using mean spectral radiative kernels reveals that this is largely due to an enhanced surface temperature feedback (STF) which is caused by a drier atmosphere and stronger surface warming compared to the CMIP6 models. The total feedback parameter in the atmospheric window (λ_{AW}) is almost solely determined by the STF for constant column relative humidity (CRH) under warming. However, most models analysed feature a decrease in CRH, which results in negative net atmospheric feedback contributing significantly to λ_{AW}.

In the H_2O absorption bands in the MIR and FIR, changes in upper tropospheric relative humidity (RH) with temperature seem to be the determining factor for λ_ν. Hereby, decreasing RH is associated with a more negative λ_ν, while constant RH results in a close to zero λ_ν. This study demonstrates how the spectral decomposition of λ into λ_ν can be employed to infer details about how different climate feedbacks operate.

Contents

Acronyms

ADM	angular distributions model
AF	net atmospheric feedback
ATF	atmospheric temperature feedback
AVHRR	Advanced Very High Resolution Radiometer
AW	atmospheric window
CH_4	methane
CMIP	Coupled Model Intercomparison Project
CMIP6	Coupled Model Intercomparison Project Phase 6
CO_2	carbon dioxide
CRH	column relative humidity
ECS	equilibrium climate sensitivity
ENSO	El Niño Southern Oscillation
ERA5	ECMWF Reanalysis v5
FIR	far-infrared
FORUM	Far-infrared-Outgoing-Radiation Understanding and Monitoring
GLQ	Gauss-Legendre Quadrature
H_2O	water vapour
IASI	Infrared Atmospheric Sounding Interferometer
IWV	integrated water vapour
LRF	lapse rate feedback
Metop	meteorological operational satellite
MIR	mid-infrared
MSRK	mean spectral radiative kernel
N_2O	nitrous oxide
OLR	outgoing longwave radiation
O_3	ozone
PF	Planck feedback

RCE radiative-convective equilibrium

RH relative humidity

RTTOV Radiative Transfer for TOVs

SST sea surface temperature

STF surface temperature feedback

TOA top of the atmosphere

WVF water vapour feedback

1 Introduction

Constraining Earth's equilibrium climate sensitivity (ECS) is one of the central challenges in climate science. It defines how much the global mean near-surface temperature T_S rises if exposed to the forcing from doubling the atmospheric CO_2 concentration $F_{2\times CO_2}$. It is written as

$$\mathrm{ECS} = -\frac{F_{2\times CO_2}}{\lambda}, \tag{1.1}$$

where λ (in W m^{-2} K^{-1}) is the climate feedback parameter. It is in turn defined as

$$\lambda = \frac{dR}{dT_S}, \tag{1.2}$$

where R is the (positive downwards) net radiative flux at top of the atmosphere (TOA) (Gregory et al., 2004). A negative feedback parameter is thus needed for a stable climate. Most of the uncertainty in ECS arises from uncertainties in λ, which is why constraining λ is of such paramount importance.

A number of different approaches have been used to estimate both ECS and λ. Those approaches include observational records (e. g., Roe and Armour, 2011), data from paleo-proxies (e. g., Friedrich and Timmermann, 2020) and climate models of varying complexity (e. g., Williams et al., 2008; Danabasoglu and Gent, 2009; Kluft et al., 2019). There have also been investigations combining those different lines of evidence to derive a probability density function for Earth's ECS (e. g., Sherwood et al., 2020).

Nevertheless, most studies limit their investigation to the integrated λ, ignoring its substantial spectral variation. Huang et al. (2014) showed that investigating the spectral feedback parameter

$$\lambda_\nu = \frac{dR_\nu}{dT_S} \tag{1.3}$$

allows a more thorough analysis of the vertical distribution of climate feedbacks. This is due to the absorption strength strongly varying with wavenumber ν, affecting the effective emission level and hence causing different parts of the spectrum to be sensitive to different atmospheric layers. He also showed that the spectral decomposition can reveal compensating feedback processes, where climate models might have similar overall λ even though their λ_ν varies significantly in some spectral regions. Therefore, a better understanding of λ_ν helps in assessing uncertainties in the underlying feedback mechanisms such as the water vapour feedback (WVF) and lapse rate feedback (LRF) and from which atmospheric layer they originate.

Furthermore, most analyses infer λ from warming caused by external forcing. While this

is a very straightforward approach, it has the downside of requiring relatively long time periods for the warming signal to be significantly larger than the interannual variability. A different approach uses those interannual variations of R and temperature directly to infer the integrated λ, requiring only a few years of data (Dessler, 2013; Proistosescu et al., 2018; Dessler and Forster, 2018).

Recently, it was suggested that the atmospheric temperature at 500 hPa T_A is more suitable for calculating λ from interannual variability compared to using T_S. One of the main reasons is that the interannual variations of T_S are dominated by the El Niño Southern Oscillation (ENSO), which exhibits a much more heterogeneous spatial pattern compared to the response of T_S to forcing. Due to the much more homogeneous distribution of T_A, it correlates better with R (Dessler et al., 2018).

I combine the approaches by Huang et al. (2014) and Dessler et al. (2018), developing a method for inferring λ_ν for longwave clear-sky feedbacks over the tropical ocean from interannual variability. I investigate, whether it is possible to derive λ_ν by using hyperspectral satellite measurements of interannual variations in the spectral outgoing longwave radiation (OLR_ν) and T_A. Therefore, I infer λ_ν from those variations as observed by the Infrared Atmospheric Sounding Interferometer (IASI). Unfortunately, its spectral coverage does not include the FIR H_2O band, where a significant part of the OLR is emitted. This gap will be filled by the Far-infrared-Outgoing-Radiation Understanding and Monitoring (FORUM) mission which will deliver hyperspectral observations of the FIR (Blumstein et al., 2004; Domínguez et al., 2020). In order to be able to infer the full longwave λ_ν, I simulate observations for the IASI and FORUM spectral ranges, based on temperature and humidity profiles of different CMIP6 models using the Radiative Transfer for TOVs (RTTOV) fast code (Saunders et al., 2018), covering more than 10,000 channels between 100 and 2760 cm^{-1}.

The so inferred λ_ν are then analysed regarding their spectral signatures. A feedback decomposition based on mean spectral radiative kernels is employed to assess the varying importance of different feedback processes in different spectral bands. The spectral fingerprints of the varying model response patterns (impacting the models' representation of different feedbacks) can be quantified to explain inter-model differences in λ_ν. This method also allows an evaluation how those patterns compare to the real world by also applying it to the IASI observations, using the ECMWF Reanalysis v5 (ERA5).

Ch. 2 further discusses the theoretical background of spectral climate feedbacks and the interannual variability method. Ch. 3 gives information on the data sets from models and instruments used, while Ch. 4 describes the newly developed method as well as the analysis tools used in detail. The results are presented and discussed in Ch. 5 with a special focus on three selected spectral bands of interest, namely the atmospheric window (AW) as well as the H_2O absorption bands in the mid-infrared (MIR) and far-infrared (FIR). I conclude in Ch. 6.

2 Spectral climate feedbacks from interannual variability

In this chapter, the theoretical background of this thesis is discussed in more detail. This involves a brief introduction into the most important clear-sky feedback processes and their interactions (Sec. 2.1). It also includes a discussion about the spectrum of the outgoing longwave radiation (OLR) OLR and how the radiative properties of the atmosphere vary with wavenumber (Sec. 2.2). Finally, the upsides and challenges of using interannual variability for inferring λ in general and λ_ν in particular are explored (Sec. 2.3).

2.1 Climate feedbacks

Decomposing the radiative response of the climate system to forcing into feedbacks caused by different processes has been conducted in many different studies (e. g., Hansen et al., 1984; Held and Soden, 2006; Soden et al., 2008; Feldl and Roe, 2013). Following the sign convention in feedback analysis, negative values represent stabilising feedbacks, whereas positive values represent amplifying feedbacks. This thesis focuses on longwave clear-sky feedbacks, thus there are mainly three governing feedbacks impacting the overall feedback parameter.

The first and most basic one is the so-called Planck feedback (PF). It simply arises from the strong temperature dependence of the Planck curve and states that a blackbody emits more radiation if its temperature increases. Hence, it is a strongly stabilising feedback (Feldl and Roe, 2013). In a idealised world, where the Earth uniformly warms and nothing else changes with warming, the total feedback parameter would be given by the PF. Obviously, this is not the case for the "real" Earth, most notably, due to the presence of H_2O in the atmosphere. Its saturation vapour pressure increases exponentially with temperature, following the Clausius-Clapeyron relation. Due to its properties as a potent greenhouse gas, it inhibits much of the additional radiation emitted due to the PF, causing the positive water vapour feedback (WVF) (Hansen et al., 1984).

Furthermore, the idealised assumption of uniform warming in all atmospheric layers is not fulfilled in the real atmosphere. In particular in the tropics, where the actual lapse rate closely follows the moist adiabatic lapse rate[1], which in turn has a significant temperature

[1] Recently, substantial deviations from the moist adiabatic lapse rate in the upper tropical troposphere have been found in climate models (Keil et al., 2020).

dependence. For higher (near-surface) temperatures, it becomes flatter, corresponding to stronger warming in the middle and upper troposphere compared to near-surface. Thus, those layers emit additional radiation and hence stabilise the climate. This negative lapse rate feedback (LRF) is in turn compensated by an additional WVF that goes along with this upper tropospheric warming (Held and Shell, 2012).
While the feedback analysis is usually conducted for broadband fluxes only, a spectral decomposition offers a number of advantages. Perhaps most notably, analysing λ_ν integrated over comparatively narrow spectral bands, which are sensitive to different parts of the troposphere, allows inferences on how different processes act vertically. They can also reveal compensation of feedbacks between spectral bands, where the overall λ might be very similar, in spite of significant spectral differences (Huang et al., 2014, Pan and Huang, 2018).
In this study, I mainly focus on three different spectral bands: the H_2O absorption bands in the far-infrared (FIR) and mid-infrared (MIR), respectively, as well as the MIR atmospheric window (AW). The reasons behind this selection as well as the radiative properties of those bands are presented in the following section.

2.2 Spectral bands

The focus of this thesis lies on the radiation that is emitted by Earth's surface, absorbed and re-emitted by the atmosphere and finally reaches top of the atmosphere (TOA), the so-called outgoing longwave radiation OLR. The spectral range and signature of the OLR is theoretically given by Plancks law. However, it is reduced due to the aforementioned absorption by different atmospheric species (so-called greenhouse gases), most notably H_2O and carbon dioxide (CO_2) but also methane (CH_4), nitrous oxide (N_2O), ozone (O_3) and numerous chlorofluorocarbons, producing its characteristic spectral shape (see Fig. 2.1, bottom panel). The absorption in large parts of the spectrum is so strong, that the effective emission level[2] of the spectral outgoing longwave radiation OLR_ν is located in the middle or upper troposphere, sometimes even in the stratosphere (Fig. 2.1, middle panel). As the temperatures there are much lower compared to the surface, those layers also emit much less radiation. Thus, greenhouse gas absorption significantly reduces the OLR throughout most of the infrared (Liou, 2002).
Two very interesting spectral bands are the H_2O absorption bands in the FIR and MIR, respectively (Tab. 2.1), in the following simply referred to as H_2O bands for brevity. Here, the strong absorption causes the emission level to lie between 500 and 200 hPa, whereas the surface and lower troposphere have no significant influence on OLR_ν, due to the the high optical depth ($\tau >> 1$) in those bands (Fig. 2.1, top panel). Even so, the FIR alone is responsible for about one third of the total emitted OLR. The emission in these bands is mainly controlled by H_2O, a behaviour first described by Simpson (1928a,b), which has

[2]The emission level is the height of the maximum of the temperature kernel of all atmospheric layers (K_{T_i}) and the surface (K_{SST}) (for more information on kernels see Sec. 4.2).

Table 2.1: Spectral bands used for analysis of spectral climate feedback parameter λ_ν.

band	spectral range (cm^{-1})
far-infrared H_2O absorption band (FIR)	100 – 550
mid-infrared atmospheric window (AW)	800 – 980, 1080 – 1200
mid-infrared H_2O absorption band (MIR)	1300 – 1900

been explored again and expanded on by Ingram (2010). The most central aspects of this framework are summarised in the following.

In both FIR and MIR, strong absorption by H_2O can be assumed the only relevant quantity determining the optical depth τ. Assuming that RH stays constant, the specific humidity — and hence τ — is a fixed function of temperature. As a direct consequence, the emission level, which is located where τ reaches approximately unity, stays at the same temperature resulting in a constant OLR. For an increase (decrease) in RH, the emission level would analogously move towards lower (higher) temperatures, decreasing (increasing) the OLR. Applying this to the feedback framework, an increase (decrease) in RH with temperature would thus lead to a net positive (negative) λ_ν in the H_2O bands.

In contrast, there are a few spectral bands, so-called atmospheric windows, where the radiation originating at the surface can escape to space comparatively unattenuated, as only weak absorption lines are located in those spectral bands. The most important window from an energetic standpoint is the mid-infrared atmospheric window (Tab. 2.1), ranging from 800 to around $1200\,\mathrm{cm}^{-1}$, only interrupted by an ozone absorption band between 980 and $1080\,\mathrm{cm}^{-1}$. It is responsible for roughly 25 % of the total OLR, highlighting its importance for Earth's ability to get rid of excess energy.

The atmospheric window is optically thin with an optical depth of $\tau \approx 1$ (Fig. 2.1, top panel), the emission level is situated close to or at the surface (middle panel). The OLR_ν (bottom panel) closely follows the Planck curve of Earth's surface temperature, but is somewhat reduced due to the H_2O continuum absorption (Liou, 2002). Hence, the emitted radiation in the atmospheric window is controlled by surface temperature and the amount of absorption aloft.

As the focus of this thesis is on tropospheric processes, spectral bands with emission levels in the stratosphere are not included in the analysis. This includes most prominently the CO_2 absorption band at around 600–$750\,\mathrm{cm}^{-1}$, as well as the ozone absorption band at around 980–$1080\,\mathrm{cm}^{-1}$. Absorption bands of other greenhouse gases (mainly CH_4 and N_2O) are also not discussed. Finally, spectral regions above $2000\,\mathrm{cm}^{-1}$ are also not analysed further, as only very little terrestrial radiation is emitted there, causing negligible λ_ν.

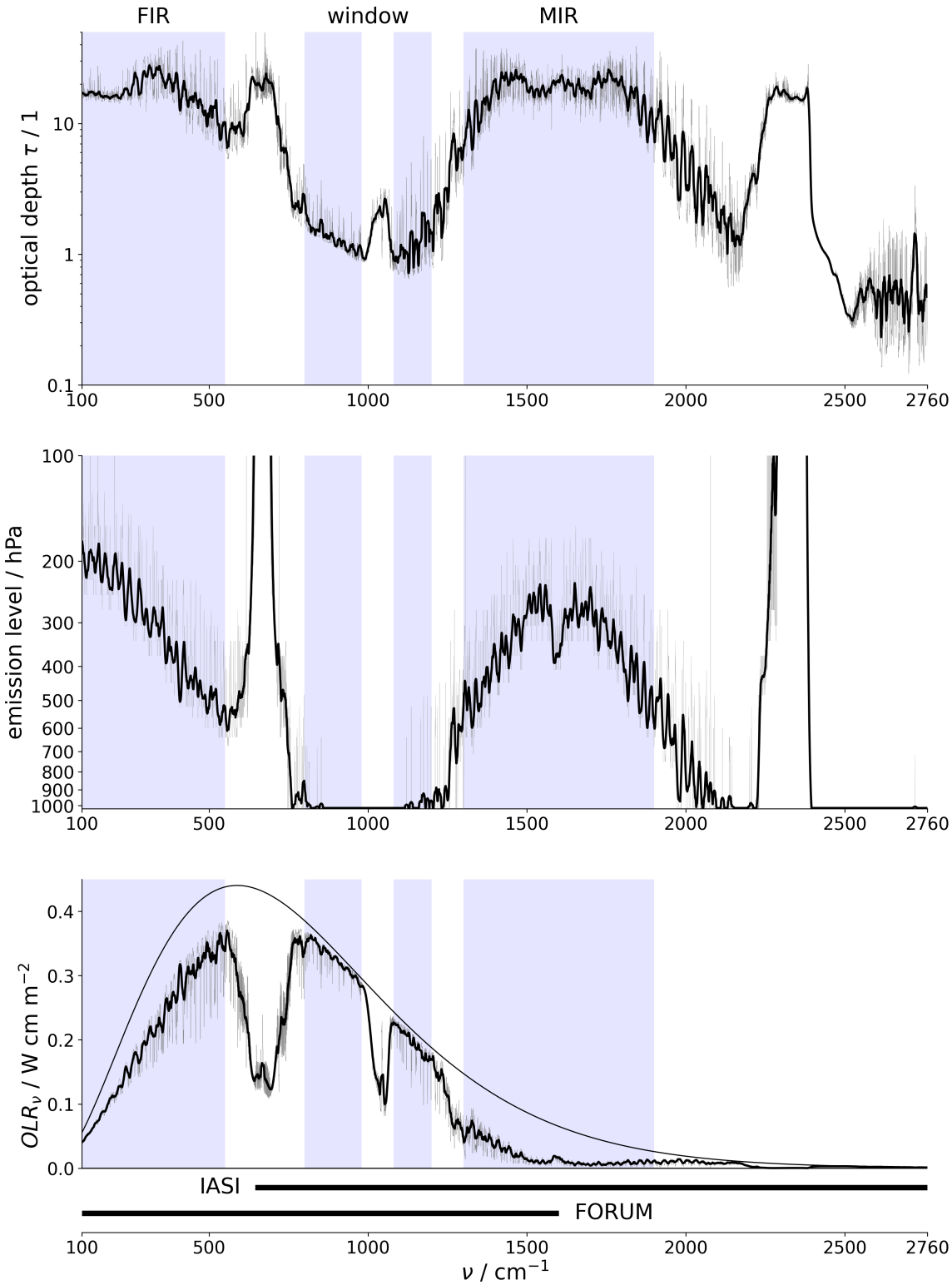

Figure 2.1: Radiative properties of the atmosphere (calculated using RTTOV): high spectral resolution (grey) and the 10 cm^{-1} moving average (black). The spectral bands of interest are labelled and shaded blue. The spectral coverage of the IASI and FORUM instruments are also indicated. Optical depth τ (top panel), emission level (middle panel) and outgoing longwave radiation (OLR), with a reference Planck curve of the mean SST (300K) (bottom panel) are shown.

2.3 Interannual variability

There have been many studies investigating the connection between the climate feedback parameter λ inferred from forced warming and that derived from interannual variability (e. g., Proistosescu et al., 2018; Dessler and Forster, 2018; Dessler et al., 2018; Sherwood et al., 2020). The latter approach requires much less data, already ten years have been shown to be sufficient (Dessler, 2013). Nevertheless, there are a couple of challenges that arise.

As the interannual variations of the near-surface temperature T_S are dominated by the El Niño Southern Oscillation (ENSO), the observed patterns are very spatially heterogeneous, with greater warming in the eastern Pacific compared to the western Pacific. This is not in principle dissimilar from near-surface warming caused by external forcing, which exhibits an "ENSO-like" pattern (Meehl and Washington, 1996; Sherwood et al., 2020). The interannual variations are, however, more heterogeneous compared to the warming under greenhouse gas forcing. This in turn can, due to non-linearities in radiative transfer, impact OLR even if the mean T_S does not change. This causes the λ derived from interannual variability (λ_{iv}) to be inherently different from that of a forced warming (λ_{forced}) (Dessler and Forster, 2018; Dessler et al., 2018).

This is why it was suggested to use the more spatially homogeneous atmospheric temperature at 500 hPa T_A as regression variable. The reason is that, as most of the OLR is not emitted at the surface but rather further up in the troposphere, T_A is a more representative reference, causing a regression of R against T_A to have a higher correlation coefficient compared to T_S. The above mentioned difference between λ_{iv} and λ_{forced} is also substantially smaller for this approach (Dessler and Forster, 2018; Dessler et al., 2018).

For the spectral decomposition conducted in this thesis, the considerations are somewhat more nuanced. T_A seems to be the better quantity determining λ_ν in spectral regions subject to strong greenhouse gas absorption (mainly the H_2O bands). Yet, the picture looks somewhat different in the atmospheric window, where a significant part of the total OLR is emitted. The radiation there originates very close to the surface, making T_S the more representative reference temperature. However, as mentioned, the near-surface heterogeneity might also cause the regression against T_S to be erroneous.

Overall, T_A delivers the smaller regression errors, in particular in the H_2O bands. Keeping the already quite large uncertainty there as small as possible is therefore prioritised over further reducing the already small uncertainty in the atmospheric window.

Using T_A for the regression necessitates applying a scaling factor, because the equilibrium responses of T_S and T_A differ significantly due to the lapse rate feedback (LRF), with T_A featuring significantly stronger warming than T_S. The corresponding λ (or λ_ν) derived from a regression against T_A is hence inherently smaller compared to using the traditional reference T_S. To mitigate this, the calculated λ (or λ_ν) must be scaled by a factor accounting for those different equilibrium responses (Dessler et al., 2018). This is further discussed in Sec. 4.1.

3 Data and instruments

Data from several different sources are used in this thesis. This includes both output from models of different complexities as well as satellite observations. This chapter gives some context about the data sources as well as detailed information on the exact data sets used.

CMIP6 models: The Coupled Model Intercomparison Project (CMIP) is organised by the Working Group on Coupled Modelling (WGCM), which is part of the World Climate Research Programme (WCRP). It serves to compare the performance of different coupled climate models regarding different standardised experiment setups and is currently in it's sixth phase (CMIP6). To make experiment outcomes comparable throughout different CMIP phases, the Diagnostic, Evaluation and Characterization of Klima (DECK) was introduced. It consists of four different experiments: an atmospheric simulation with prescribed historical sea surface temperatures SST (amip), a pre-industrial control simulation, where greenhouse gases are kept constant (piControl), a run where CO_2 is quadrupled abruptly (abrupt-4xCO2) and one where CO_2 is increased exponentially by 1 % every year (1pctCO2). Additionally, CMIP organises historical simulations, which try to reproduce the time from 1850 to present (Eyring et al., 2016).
Out of all the CMIP6 models delivering suitable output of the historical experiment, simulations for the years 2005–2014 (Eyring et al., 2016) from three different models are selected, for which daily profiles of temperature and specific humidity with a vertical resolution of at least 50 vertical levels are available. The latter is important to minimise errors introduced by the internal interpolation in the radiative transfer simulations (Hocking et al., 2019). The simulation setup is further described in Sec. 4.1.1.
The selected models and their horizontal resolutions are listed in Tab. 3.1. The analysis is performed based on 200 profiles per day for every CMIP6 model (about 730,000 profiles over the ten year period). The profiles are randomly selected out of all available profiles over the tropical ocean (30°S–30°N).

Table 3.1: CMIP6 models selected for the analysis with their respective modelling centre and horizontal resolution.

model	modelling centre	resolution
MPI-ESM1-2-HR	Max Planck Institute for Meteorology	$\sim 0.94° \times 0.94°$
CESM2-WACCM	National Center for Atmospheric Research	$\sim 0.94° \times 1.25°$
MRI-ESM2-0	Meteorological Research Institute	$1.125° \times 1.125°$

konrad: The 1-D model konrad was developed by Kluft et al. (2019) and Dacie et al. (2019), providing an idealised representation of the tropical atmosphere under the assumption of radiative-convective equilibrium (RCE). In this thesis, λ_ν calculated from konrad v0.8.1 (Kluft and Dacie, 2021) is used as a reference value for the analysis. It is calculated using the line-by-line radiative transfer model ARTS (Eriksson et al., 2011; Buehler et al., 2018) for a fixed, vertically constant relative humidity of 55 % (data provided by Lukas Kluft).

ERA5 reanalysis: The ECMWF Reanalysis v5 (ERA5), created by the European Centre for Medium-Range Weather Forecasts (ECMWF), provides a detailed, global record of the state of atmosphere, ocean and land surface from 1979 to present day. Compared to its predecessor ERA-Interim it has a much higher horizontal resolution of 31 km. By combining modelling and observations, it provides robust and consistent information on a large number of atmospheric fields (Hersbach et al., 2020).
From ERA5, I use monthly mean values of sea surface temperature (SST) (for the years 2007–2020) and near-surface temperature T_S (2010–2019) (Hersbach et al., 2019a) as well as profiles of temperature and specific humidity for the years 2010–2019 (Hersbach et al., 2019b). For all datasets mentioned, the tropical latitudes (30°N – 30°S) are selected.

Satellite observations: The meteorological operational satellites (Metop A, B and C), launched in 2006, 2012 and 2018, respectively, are part of the EUMETSAT Polar System (EPS). They provide meteorological data in real time on the sun-synchronous morning orbit (09:30 local solar time, descending node).
One of the key instruments on board is the Infrared Atmospheric Sounding Interferometer (IASI). It provides hyperspectral measurements of emitted spectral radiances in the thermal infrared (645–2760 cm^{-1}, 3.7-–15.5 μm) with a spectral sampling of 0.25 cm^{-1} and a spectral resolution after apodisation of 0.5 cm^{-1} (Blumstein et al., 2004; August et al., 2012; Righetti et al., 2020). The absolute brightness temperature radiometric accuracy was found to be between 0.2 and 0.5 K, with an accuracy of up to 0.1 K for some wavelengths (Illingworth et al., 2009; Larar et al., 2010). IASI scans across-track with a field of view of $\pm 48.33°$ relative to nadir, corresponding to a swath width on ground of 2200 km, which ensures global coverage twice a day. The highest horizontal resolution is reached directly below the satellite, with an instantaneous field of view of 12 km (August et al., 2012).
Another instrument onboard Metop is the Advanced Very High Resolution Radiometer (AVHRR). It features six different channels in the visible and infrared and measures with a horizontal resolution of 1.1 km. This way, it can provide binary masks on cloudiness and surface type. Its results are averaged over the IASI footprint, resulting in the AVHRR cloud fraction and land/sea mask products, respectively, which are included in the IASI level 1c (L1C) data (Klaes et al., 2007; August et al., 2012; Bouillon et al., 2020).

I use the IASI L1C data from the Metop A satellite, including the AVHRR land/sea mask and cloud-fraction (EUMETSAT, 2018). The vast amount of IASI data available proved challenging, as one month of data alone takes up almost 1 TB in disk space. Due to limitations in available disk space and computing time for processing, and in particular because of the necessity of data transfer, it was not possible to analyse the desirable full ten years from 2010 to 2019.
Instead, based on the yearly tropical mean SST from ERA5 between 2007 and 2020, only the years with the highest and lowest averages as well as the 33rd and 67th percentiles were selected. This selection corresponds to the years 2011, 2013, 2017 and 2016, respectively. This way, it was ensured to both optimise the signal to noise ratio, while at the same time not solely relying on extremes. To further reduce the amount of data, the yearly means were approximated by only using the odd numbered months (January, March, May, July, September and November) of the selected years.

4 Methods

The newly developed method for inferring λ_ν from interannual variability is described in this chapter. This involves first and foremost the formula used for the inference and the domain in which it is applied. Additionally, the setup of the radiative transfer simulation as well as the calculation of the spectral fluxes F_ν from the available spectral radiances L_ν is described for both simulations and observations. Finally, the mean spectral radiative kernel (MSRK) method is discussed as an analysis tool for feedback decomposition.

4.1 New method for inferring spectral feedback parameter

I develop a new method for inferring spectral climate feedback parameter λ_ν from interannual variability (iv). In this study, only the longwave (lw) part of λ_ν is considered, thus the spectral net radiative flux R_ν at top of the atmosphere (TOA) in Equation (1.3) is replaced by the spectral outgoing longwave radiation (OLR_ν) between 100 and 2760 cm^{-1}. Annual averages of OLR_ν are regressed against the annual mean atmospheric temperature at 500 hPa T_A. For simplicity, it is only applied to clear-skies (cs) over the tropical ocean (troc) (30°S–30°N), yielding

$$\lambda_{\nu,\,\mathrm{troc,\,lw,\,cs,\,iv}} = -\frac{dOLR_\nu}{dT_\mathrm{A}}\frac{\Delta T_\mathrm{A}}{\Delta T_S}, \tag{4.1}$$

which in the following is simply written as λ_ν for brevity.
The derivative of OLR_ν with respect to T_A is calculated using a linear least-squares regression based on annual means for each wavenumber ν. I account for the different equilibrium warmings of T_A and the near-surface temperature T_S by applying a scaling factor $\frac{\Delta T_\mathrm{A}}{\Delta T_\mathrm{S}}$. It is derived from the ratios of the respective warmings within the first 150 years of the 4xCO2 experiment of the three analysed CMIP6 models. Those warmings (ΔT_A and ΔT_S) are in turn calculated from the differences between the first and last decade in that time period and then averaged over the three analysed CMIP6 models. This yields a value for the scaling factor of $\frac{\Delta T_\mathrm{A}}{\Delta T_\mathrm{S}} = 1.385\ \mathrm{K\,K^{-1}}$, which is equally applied to all models as well as to the IASI observations[1].

[1] For reference, Dessler et al. (2018) used the first and last decades of the 4xCO2 experiment and calculated the ratio between the tropical T_A and global T_S, yielding $\frac{\Delta T_\mathrm{A}}{\Delta T_\mathrm{S}} = 1.16\ \mathrm{K\,K^{-1}}$.

4.1.1 Radiative transfer simulation

The simulations in this thesis are conducted using version 12.2 of the fast radiative transfer model Radiative Transfer for TOVs (RTTOV). It allows simulations of outgoing spectral radiances L_ν as observed by satellite instruments and covers the the visible, infrared and microwave spectral ranges (Saunders et al., 2018). This makes it a useful tool for satellite retrievals (Meng et al., 2016) and data assimilation in numerical weather prediction (Pavelin et al., 2008).

The simulations cover 10278 channels between 100 to 2760 cm^{-1}. It includes both the 8461 channels of the Infrared Atmospheric Sounding Interferometer (IASI) (645–2760 cm^{-1}, with a spectral sampling of 0.25 cm^{-1}, see Ch. 3), as well as the part of the spectral range of the future Far-infrared-Outgoing-Radiation Understanding and Monitoring (FORUM) mission, which is not covered by IASI (100–645 cm^{-1}, with a spectral sampling of 0.3 cm^{-1}) (Blumstein et al., 2004; Domínguez et al., 2020).

Daily profiles of temperature T and specific humidity q as well as sea surface temperatures SST from three different CMIP6 models performing the historical experiment serve as input (see Ch. 3). Additionally, near-surface values of T, q, wind components u and v and air pressure p are provided, as well as surface type (land/sea mask), surface elevation and sea ice concentration (zero in the tropics). As I only perform clear-sky simulations, the cloud liquid content is set to zero. Not all CMIP6 models have interactive chemistry, some get their concentrations for gases like ozone (O_3) from databases (Maycock, 2016). To ensure comparability between the models and since the focus of this thesis lies on tropospheric processes, where O_3 only plays a minor role, RTTOV's internal O_3 climatology is used for the simulations (Hocking et al., 2019).

The model output profiles provided represent the average value over the respective vertical layer. RTTOV, however, requires values for the exact levels. Thus, the layer values are interpolated (in log pressure) to the layer bounds. As the pressure in the lowest layer is significantly lower than surface pressure for some models, the near-surface values of p, T and q are used to calculate profiles starting at the surface.

CESM2-WACCM's uppermost layers are located within the thermosphere, where temperatures of more than 400 K are reached, beyond the upper limit RTTOV allows for its simulations. Therefore, those levels are excluded, using the 1 Pa pressure level as a cut-off for all models. This mainly affects CESM2-WACCM, but also the uppermost level of MRI-ESM2-0, as shown in Table 4.1.

The models are kept at their respective vertical resolutions for the radiative transfer simulations using the forward model, although RTTOV performs internal interpolation to its native grid. An exception is the calculation of the mean spectral radiative kernel (MSRK), using RTTOV's Jacobian model (Hocking et al., 2019). To allow level-wise intercomparison between the models, the profiles are interpolated to MRI-ESM2-0's vertical coordinates, which feature the most levels in the troposphere.

Table 4.1: Vertical resolution of analysed models: total number of vertical levels and number of used vertical levels.

model	total # of vertical levels	# of used vertical levels
MPI-ESM1-2-HR	95	95
CESM2-WACCM	70	56
MRI-ESM2-0	81	80

4.1.2 Flux calculation

Both simulation and observations deliver spectral radiances L_ν, which need to be converted into spectral fluxes F_ν for inferring λ_ν. Both quantities are linked by the equation

$$F_\nu = \int_{\theta=0}^{\pi/2} \int_{\phi=0}^{2\pi} L_\nu(\theta, \phi) \cos(\theta) \sin(\theta)\, d\theta\, d\phi, \tag{4.2}$$

where θ and ϕ represent the zenith and azimuth angles, respectively (Whitburn et al., 2020). Assuming azimuthal symmetry, Equation (4.2) reads as

$$F_\nu = 2\pi \int_{\theta=0}^{\pi/2} L_\nu(\theta) \cos(\theta) \sin(\theta)\, d\theta. \tag{4.3}$$

Substituting $\mu = \cos(\theta)$, this can be rewritten as

$$F_\nu = 2\pi \int_0^1 L_\nu(\mu)\, \mu\, d\mu. \tag{4.4}$$

Radiative transfer simulations

A widely used technique for approximating radiative fluxes from radiances is the so-called Gauss-Legendre Quadrature (GLQ) (Liang and Strahler, 1993; Li and Barker, 2018). It is a powerful tool for approximating the integral of a function $f(\mu)$ with high accuracy. For any (finite) interval [a, b], f is approximated using an optimised set of n sample points μ_i with corresponding weights w_i, reading

$$\int_a^b f(\mu)\, d\mu \approx \sum_{i=1}^{n} w_i\, f(\mu_i). \tag{4.5}$$

The sample points μ_i and weights w_i are calculated by

$$\begin{aligned} \mu_i &= \frac{a + b + (b - a)\xi_i}{2} \\ w_i &= \frac{b - a}{(1 - \xi_i)^2 [P_n'(\xi_i)]^2}. \end{aligned} \tag{4.6}$$

The ξ_i are the Gauss points for the interval [-1, 1], corresponding to the zeros of the Legendre Polynomials P_n of degree n in the same interval (Kythe and Puri, 2011).

Table 4.2: The sample points μ_i with corresponding weights w_i and zenith angles θ_i for the applied two-angle GLQ.

i	μ_i	w_i	θ_i
1	0.78867513	0.5	37.93812743°
2	0.21132487	0.5	77.79999596°

Applying a two-angle GLQ to Equation (4.4), F_ν can be approximated as

$$F_\nu \approx 2\pi \sum_{i=1}^{2} L_\nu(\mu_i)\, \mu_i\, w_i. \tag{4.7}$$

The used values[2] for the μ_i and w_i are listed in Tab. 4.2, together with the corresponding zenith angles $\theta_i = \arccos(\mu_i)$. Because RTTOV only allows simulations for $\theta \leq 75°$, $L_\nu(75°)$ is simulated instead of $L_\nu(\theta_2)$. The latter is then inferred from a linear interpolation of $L_\nu(\theta)\cos(\theta)$, using the boundary condition $L_\nu(90°)\cos(90°) = 0$.

Satelllite observations

Numerous studies have developed algorithms of varying complexity for estimating radiative fluxes from radiances for different satellite instruments (e. g., Suttles et al., 1989; Clerbaux et al., 2003; Loeb et al., 2005; Kato and Loeb, 2005). A very common approach is to calculate empirical angular distributions models (ADMs), which are derived separately for a number of different scene types.

A comprehensive spectral method for inferring F_ν from IASI measurements is described in Whitburn et al. (2020). They create a large set of different scene types that vary in their concentration of different greenhouse gases, as well as their temperature profiles and surface temperatures. They then use forward modelling to derive spectral ADMs for every scene type, from which they infer F_ν.

In this thesis, a simplified approach is chosen. The land/sea mask and cloud-fraction products from AVHRR (see Ch. 3) are used to filter out clear-sky pixels over the tropical ocean. Instead of differentiating every filtered IASI pixel based on their atmospheric conditions, all observed L_ν within one IASI orbit (each corresponding to just under two hours of observations) are used together to calculate one mean F_ν.

To achieve this, the L_ν of the filtered pixels are sorted into 5° bins with respect to θ. IASI's limited field of view (see Ch. 3) obviously limits the instruments maximum zenith angle θ as seen from Earth, to a $\theta_{\text{max, IASI}}$ of about 58.7°. Therefore, the product $L_\nu(\theta)\cos(\theta)$ is averaged over each bin and then linearly interpolated for θ greater than $\theta_{\text{max, IASI}}$. Finally, integration over all θ yields mean F_ν for every IASI orbit, which are then averaged annually.

[2]They were calcualted using the numpy.polynomial.legendre.leggauss function provided by the numpy package (Harris et al., 2020) to calculate the respective values in the interval [-1, 1] and then converting them to the interval [0, 1], following Equation (4.6).

4.2 Mean spectral radiative kernel technique

The radiative kernel technique was introduced by Held and Soden (2006) and Soden et al. (2008) and has since been widely used as an analysis tool in climate feedback analysis (e. g., Shell et al., 2008; Sanderson et al., 2010; Pendergrass et al., 2018). The basic idea is to evaluate the "climate-response patterns" and the corresponding broadband "radiative kernels" with high temporal resolution to derive decomposed Planck feedback (PF), water vapour feedback (WVF) and lapse rate feedback (LRF) by averaging and then multiplying them. A similar spectral radiative feedback kernel was developed by Huang et al. (2014), replacing broadband with spectral radiative kernels, and was also used by Pan and Huang (2018).

In this thesis, mean spectral radiative kernels (MSRKs) are constructed for decomposing λ_ν into its main feedbacks, to investigate which processes are responsible for differences in λ_ν between the different models. For computational efficiency, this is done by calculating the corresponding kernels K_x only for the respective model mean state variables x (profiles of temperature T and specific humidity q, as well as sea surface temperature SST). The simulations and flux computation are conducted as described in Secs. 4.1.1 and 4.1.2, respectively. The response patterns with changing atmospheric temperature at 500 hPa T_A, $\frac{\partial x}{\partial T_\mathrm{A}}$ (in the following simply $\partial_{T_\mathrm{A}} x$), are calculated by performing linear least-square regression of their yearly means. To analyse the IASI observations, the respective quantities from ERA5 are used for the months from which IASI observations were selected (see Ch. 3). Following the framework described above, λ_ν for a model with N vertical levels can be approximated as

$$\begin{aligned}\lambda_\nu \propto -\frac{dOLR_\nu}{dT_\mathrm{A}} &\approx -\overbrace{\frac{\partial OLR_\nu}{\partial \mathrm{SST}}}^{K_\mathrm{SST}} \frac{\partial \mathrm{SST}}{\partial T_\mathrm{A}} - \sum_{i=1}^{N} \overbrace{\frac{\partial OLR_\nu}{\partial T_i}}^{K_{T_i}} \frac{\partial T_i}{\partial T_\mathrm{A}} - \sum_{i=1}^{N} \overbrace{\frac{\partial OLR_\nu}{\partial q_i}}^{K_{q_i}} \frac{\partial q_i}{\partial T_\mathrm{A}} \\ &= \underbrace{-K_\mathrm{SST}\, \partial_{T_\mathrm{A}} \mathrm{SST}}_{\mathrm{STF}} \underbrace{- \sum_{i=1}^{N} K_{T_i}\, \partial_{T_\mathrm{A}} T_i}_{\mathrm{ATF}} \underbrace{- \sum_{i=1}^{N} K_{q_i}\, \partial_{T_\mathrm{A}} q_i}_{\mathrm{WVF}}\end{aligned} \tag{4.8}$$

This way, λ_ν is decomposed into three main feedbacks: The first term (surface temperature feedback, STF) represents the change in the spectral outgoing longwave radiation (OLR_ν) due to changes of the Earth's surface temperature[3] with T_A, corresponding to the surface component of the stabilising PF. The second term (atmospheric temperature feedback, ATF) is analogously the change in OLR_ν due to changes of the atmospheric T profile, including the rest of the PF as well as the LRF. Finally, the third term (water vapour feedback, WVF) encompasses the change in OLR_ν due to changing the atmospheric q profile, as described in Sec. 2.1.

[3] As only spectra over the ocean are considered, the surface temperature is equivalent to the sea surface temperature SST.

5 Results and discussion

This chapter shows the results for the spectral feedback parameters λ_ν inferred using the newly developed method described in Sec. 4.1. Their broadband values are briefly analysed and compared with results from a well-established method (Sec. 5.1). The main focus lies on the spectral dependence of λ_ν, which is analysed in detail with regard to both integrated values of the spectral bands as well as their detailed spectral shape. The focus of the investigation lies mainly on the three spectral bands described in Sec. 2.2, namely the atmospheric window (AW) (Sec. 5.2.1) and the H_2O bands in the mid-infrared (MIR) and far-infrared (FIR) (Sec. 5.2.2). Nevertheless, the ozone absorption band is also briefly discussed (Sec. 5.2.3).

5.1 Broadband analysis

The integrals of λ_ν over the whole spectral range (λ) as well as over the range covered by IASI (λ_{IASI}) are shown in Tab. 5.1 for the different considered data sets. They are more negative than the estimate of the total global λ by Sherwood et al. (2020), which also includes shortwave, extra-tropical and cloud feedbacks. Still, with the exception of CESM2-WACCM, they all lie within the uncertainty interval given. The λ of MRI-ESM2-0 is closest to that of konrad, whereas MPI-ESM1-2-HR has the least negative λ and CESM2-WACCM has the most negative λ. Over the spectral range covered by IASI, the CMIP6 models (as well as konrad) have much less negative values compared to IASI.

Table 5.1: Inferred λ_ν integrated over the whole simulated spectral range (λ, 100–2760 cm^{-1}) and over the spectral range covered by IASI (λ_{IASI}, 645–2760 cm^{-1}) from all considered data sets. As reference, mean and standard deviation of the total global λ as derived by Sherwood et al. (2020) are also shown.

	λ (W m^{-2} K^{-1})	λ_{IASI} (W m^{-2} K^{-1})
MPI-ESM1-2-HR	-1.43	-1.16
CESM2-WACCM	-1.93	-1.23
MRI-ESM2-0	-1.62	-1.00
IASI	–	-1.59
konrad	-1.64	-1.19
Sherwood et al. (2020)	-1.30 $\pm$ 0.44	–

It is instructive to compare the λ of the three used CMIP6 models derived from interannual variability (λ_{iv}) to that for a forced warming ($\lambda_{\mathrm{forced}}$) calculated for the same models using a method introduced by Gregory et al. (2004)[1].
For comparability, both methods are applied to the same domain (clear-sky outgoing longwave spectra over the tropical ocean) and regressed against the atmospheric temperature at 500 hPa T_{A}. Instead of the net radiative flux R, I thus use the broadband clear-sky outgoing longwave radiation OLR of the respective CMIP6 models from the 4xCO2 experiment.
Both methods produce quite similar results (Tab. 5.2), with λ_{iv} being slightly less negative on average, even though it is more negative for CESM2-WACCM. For all three models, the difference between the two methods is smaller than 0.2 W m^{-2} K^{-1}, and even smaller than 0.1 W m^{-2} K^{-1} for MPI-ESM1-2-HR and CESM2-WACCM. The order of the models from smallest to largest λ is also retained between both methods. However, the $\lambda_{\mathrm{forced}}$ for MRI-ESM2-0 and CESM2-WACCM are almost identical, while CESM2-WACCM features a 0.3 W m^{-2} K^{-1} more negative λ_{iv}. All in all, the comparison shows hat the interannual variability method accurately captures λ, delivering results rather similar to the well-established method of Gregory et al. (2004).

Table 5.2: Climate feedback parameter derived from interannual variability (λ_{iv}) and from forced warming ($\lambda_{\mathrm{forced}}$).

model	λ_{iv} (W m^{-2} K^{-1})	$\lambda_{\mathrm{forced}}$ (W m^{-2} K^{-1})
MPI-ESM1-2-HR	-1.43	-1.53
CESM2-WACCM	-1.93	-1.84
MRI-ESM2-0	-1.62	-1.80
mean	-1.66	-1.72

5.2 Spectral analysis

The inferred λ_ν for the three analysed CMIP6 models as well as the IASI observations and konrad are shown spectrally resolved in Fig. 5.1. Contrary to the broadband λ, quite significant differences between the CMIP6 models are revealed in the spectral decomposition. IASI's more negative integral over its range of spectral coverage (λ_{IASI}) compared to the CMIP6 models (see Sec. 5.1) seems to mainly result from IASI's more negative λ_ν in the atmospheric window (AW) between 800 and 1200 cm^{-1}. The least negative λ of MPI-ESM1-2-HR, on the other hand, appears to be due to its close to zero λ_ν in the far-infrared (FIR) from 100 to about 500 cm^{-1}. Overall, there are many different aspects to be discussed from the central results shown in Fig. 5.1. They are discussed separately for the AW (Sec. 5.2.1) and the H_2O bands (Sec. 5.2.2).

[1] They regress the annual mean net radiative flux at TOA R against the change in near-surface temperature T_{S} for the 2xCO2 and 4xCO2 experiments. The slope of the regression delivers an estimate of $\lambda_{\mathrm{forced}}$.

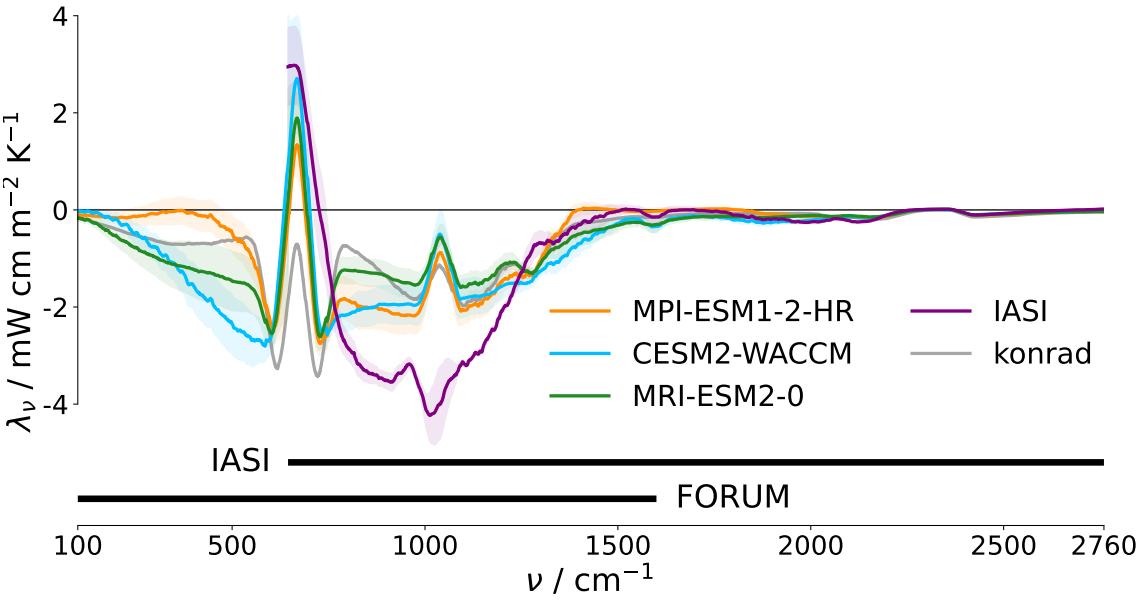

Figure 5.1: Spectral feedback parameter λ_ν (50 cm^{-1} moving average) for the CMIP6 models MPI-ESM1-2-HR (orange), CESM2-WACCM (blue) and MRI-ESM2-0 (green) as well as the RCE model konrad (grey) and based on observations by the IASI instrument (purple). The shaded areas around the curves represent the regression errors. Additionally, the spectral ranges of the current IASI and future FORUM instruments are indicated as thick black lines.

5.2.1 Atmospheric window

The values of λ_ν integrated over the whole atmospheric window (AW) for the considered data sets are shown in the first column of Tab. 5.3. They show substantial variation, with the absolute value of IASI's λ_{AW} more than twice as large as that of MRI-ESM2-0. λ_{AW} of MPI-ESM1-2-HR and CESM2-WACCM lie in between, although closer to MRI-ESM2-0, with MPI-ESM1-2-HR exhibiting the slightly more negative λ_{AW}.

The mean relative humidity of the used models, the so-called column relative humidity CRH[2], is shown in Tab. 5.4. Although all models have CRH between 54 % and 58 %, their λ_{AW} differ substantially from that of konrad (55 %). MRI-ESM2-0's λ_{AW} is very similar to konrad's, the other two CMIP6 models, however, feature substantially more negative λ_{AW}. IASI's λ_{AW} even features an absolute value more than twice that of konrad.

The most obvious difference between konrad and the other models concerns the vertical RH distribution, which has been found to affect λ, with higher RH at lower altitudes leading to more effective cooling and hence a more negative λ (Bourdin et al., 2021). RH in the konrad setup used here is vertically constant, while it has a C-shape in CMIP6 and ERA5 (Fig. 5.2). Thus, RH in CMIP6 and ERA5 is higher in the lower troposphere, partly explaining the more negative λ_{AW}.

But other factors also contribute, such as the change in RH with T_{A}, which has already

[2]CRH is defined as the ratio between the integrated water vapour IWV of an atmospheric column and the IWV for the same temperature profile under saturated conditions (Rushley et al., 2017).

Table 5.3: Inferred λ_ν integrated over the atmospheric window (λ_{AW}, $\lambda_{\mathrm{AW,\,MSRK}}$) using both (simulated) observations and MSRK methods. The CMIP6 mean refers to the mean over the three selected CMIP6 models.

model/instrument	λ_{AW} (W m^{-2} K^{-1})	$\lambda_{\mathrm{AW,\,MSRK}}$ (W m^{-2} K^{-1})
MPI-ESM1-2-HR	-0.60	-0.65
CESM2-WACCM	-0.57	-0.62
MRI-ESM2-0	-0.43	-0.42
CMIP6 mean	-0.53	-0.56
IASI	-0.93	–
ERA5 (selected months)	–	-0.81
ERA5 (2010–2019)	–	-0.73
konrad	-0.45	–

Table 5.4: Mean values of column relative humidity (CRH) and the change of CRH with atmospheric temperature at 500 hPa T_{A} ($\partial_{T_{\mathrm{A}}}$CRH).

	CRH (%)	$\partial_{T_{\mathrm{A}}}$CRH (% K^{-1})
MPI-ESM1-2-HR	54.5	-0.46
CESM2-WACCM	57.6	-0.95
MRI-ESM2-0	55.9	-0.13
ERA5 (selected months)	54.3	-0.58
ERA5 (2010–2019)	55.5	-0.70
konrad	55.0	$\pm$0.00

been found by e. g., Soden et al. (2005) and Ingram (2010). For the data sets used here, this is demonstrated in the following by decomposing λ_{AW} into its main feedbacks using the mean spectral radiative kernel (MSRK) method, as described in Sec. 4.2. The sum of all feedbacks derived this way ($\lambda_{\mathrm{AW,\,MSRK}}$) is compared to λ_{AW} to evaluate the accuracy of the decomposition (Tab. 5.3). For λ_{AW} inferred from IASI observations, the MSRK method is calculated for the mean profiles from ERA5.

ERA5 features a much more negative $\lambda_{\mathrm{AW,\,MSRK}}$ compared to the CMIP6 models, although not quite as negative as IASI's λ_{AW}. MRI-ESM2-0, on the other hand, exhibits both the least negative $\lambda_{\mathrm{AW,\,MSRK}}$ and λ_{AW}, with very similar absolute values. The $\lambda_{\mathrm{AW,\,MSRK}}$ for MPI-ESM1-2-HR and CESM2-WACCM are also similar, although slightly more negative than their respective λ_{AW}.

The overall small difference between λ_{AW} and $\lambda_{\mathrm{AW,\,MSRK}}$ indicates that the main acting processes are captured by the MSRK technique. Further analysis from the decomposed feedbacks can thus, with some constraints, also be applied to λ_{AW}. The values for the decomposed atmospheric feedbacks are shown in Tab. 5.5. The surface temperature feedback (STF) is further decomposed into its radiative kernel (K_{SST}) and model response ($\partial_{T_{\mathrm{A}}}$SST) in Tab. 5.6, as described in Sec. 4.2.

ERA5 has clearly the strongest STF, which mainly results from its strong $\partial_{T_{\mathrm{A}}}$SST and to

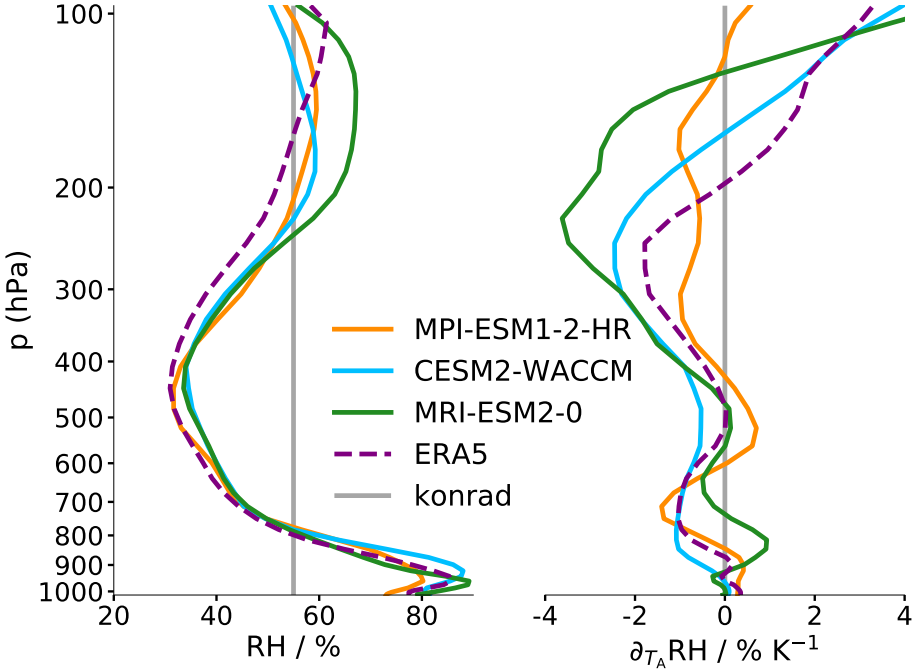

Figure 5.2: Mean profiles of RH and the change of RH with atmospheric temperature at 500 hPa (T_A) (∂_{T_A}RH).

a lesser extent from its also strong K_{SST}. On the flip side, CESM2-WACCM exhibits the weakest STF, as it both has the weakest K_{SST} and ∂_{T_A}SST. MPI-ESM1-2-HR and MRI-ESM2-0 show very similar behaviours in that regard, with MPI-ESM1-2-HR having the slightly stronger STF, due to its slightly stronger ∂_{T_A}SST.

K_{SST} is a function of atmospheric transmission and thus in turn of the integrated water vapour IWV (Koll and Cronin, 2018). Therefore, as K_{SST} generally decreases with lower transmission i. e., moister atmospheres, so should the magnitude of STF. This is confirmed comparing the values of K_{SST} and IWV for the different models. CESM2-WACCM having the highest IWV among the models appears to be responsible for its weak K_{SST} and in turn weak STF. Similarly, ERA5's relatively large K_{SST} (and thus large STF) seems to be caused by its comparatively low IWV. MPI-ESM1-2-HR and MRI-ESM2-0, finally, have very similar values of both IWV and K_{SST}.

Even though the STF makes up a large part of the total λ_{AW}, atmospheric feedbacks also contribute significantly. The net atmospheric feedback (AF) consists of contributions due to changes in the atmospheric profiles of temperature T (atmospheric temperature feedback, ATF) and specific humidity q (water vapour feedback, WVF) with warming. ERA5 also features the strongest AF, closely followed by CESM2-WACCM and then MPI-ESM1-2-HR, all having net negative AF between -0.24 and -0.31 W m^{-2} K^{-1}. The AF of MRI-ESM2-0, in contrast, is an order of magnitude smaller (-0.03 W m^{-2} K^{-1}). This close to zero AF results from the almost perfect cancellation of the significantly larger ATF and WVF, as already found by Koll and Cronin (2018). While the AF is also significantly smaller than both ATF and WVF for the other models, their ATF appears to clearly dom-

Table 5.5: Column-integrated decomposed atmospheric feedbacks integrated over the atmospheric window.

	ATF ($W\,m^{-2}\,K^{-1}$)	WVF ($W\,m^{-2}\,K^{-1}$)	AF ($W\,m^{-2}\,K^{-1}$)
MPI-ESM1-2-HR	-0.88	0.64	-0.24
CESM2-WACCM	-0.77	0.47	-0.29
MRI-ESM2-0	-0.72	0.69	-0.03
ERA5 (selected months)	-0.87	0.56	-0.31
ERA5 (2010–2019)	-0.83	0.52	-0.31

Table 5.6: Mean IWV, MSRKs integrated over AW (K_{SST}), surface warming ∂_{T_A}SST and STF. The latter results from scaling the product of the preceding two column with the derived scaling factor (see Sec. 2.3).

	IWV ($kg\,m^{-2}$)	K_{SST} ($W\,m^{-2}\,K^{-1}$)	∂_{T_A}SST ($K\,K^{-1}$)	STF ($W\,m^{-2}\,K^{-1}$)
MPI-ESM1-2-HR	39.2	-0.55	0.54	-0.41
CESM2-WACCM	41.4	-0.51	0.47	-0.33
MRI-ESM2-0	39.0	-0.55	0.51	-0.39
ERA5 (selected months)	37.3	-0.57	0.64	-0.50
ERA5 (2010–2019)	38.0	-0.56	0.54	-0.42

inate their respective WVF, causing the clearly negative AF described. This difference is not due to MRI-ESM2-0 featuring an outlier in either one of ATF or WVF. Rather, it is the result of the fact that MRI-ESM2-0 exhibits both the weakest ATF (although only slightly weaker than that of CESM2-WACCM) and the strongest WVF (although only slightly stronger than that of MPI-ESM1-2-HR).

This begs the question, why the behaviour of MRI-ESM2-0 seems to be consistent with the findings of Koll and Cronin (2018) in the cancellation of ATF and WVF, but not that of the other three models. Koll and Cronin (2018) conducted their analysis for an atmosphere saturated in all vertical levels (100 % RH). While the vertically constant RH is a strong simplification (most models analysed feature a C-shape), the assumption of constant RH under warming is broadly supported by global climate models simulations, which show only small changes in RH with warming (Ingram, 2002; Allen and Ingram, 2002). However, even small changes in RH can have significant effects on radiative balance, in particular in the upper tropical troposphere (Soden et al., 2005).

To verify, whether the mean RH of the atmospheric column also stays constant in the analysed data sets, the respective changes in column relative humidity CRHs with T_A (∂_{T_A}CRH) are calculated. The only model where ∂_{T_A}CRH is insignificantly different from zero is MRI-ESM2-0, which also features a near-zero AF, as demonstrated. Even so, both quantities are slightly negative. All the other models, which exhibit clearly negative AF, actually feature a significant decrease of CRH with warming. This causes the WVF to be too weak to balance the ATF in these models. This study does not attempt to evaluate, whether this decrease in CRH is robust, but rather focuses on how a negative ∂_{T_A}CRH,

impacts λ_v.

This now answers the question posed at the beginning of this chapter, why the analysed models (and the IASI observations) exhibit such a large spread in λ_{AW}. Even though their mean CRH are all very similar to that of konrad their λ_{AW} are (with the notable exception of MRI-ESM2-0) much more negative. This appears to be the combined effect of both different vertical distributions of RH and the decreasing CRH in the CMIP6 models and ERA5 causing negative AF. Similar to MRI-ESM2-0, the AF in konrad can be assumed to be near-zero due to its fixed RH.

The feedback decomposition also allows to pinpoint to atmospheric layers, where the differences in ATF and WVF are the largest. The vertical profiles of the state variables changes $\partial_{T_\mathrm{A}} x$, the radiative kernels K_x, as well as the resulting feedbacks integrated over the atmospheric window are shown in Fig. 5.3. Almost all of the atmospheric temperature feedback (ATF) (upper right panel) occurs below 500 hPa, with the layer between 700 and 900 hPa having the largest impact (as it is scaled by the temperature kernel K_T in the upper left panel). MRI-ESM2-0's relatively weak warming in the lower troposphere is responsible for a significantly weaker ATF between roughly 950 and 650 hPa compared to the other models. On the other hand, the comparatively strong warming of MPI-ESM1-2-HR and ERA5 there causes them to have much stronger ATF.

A similar feature can be seen in the water vapour feedback (WVF) (centre right panel). The strong increase in q in MRI-ESM2-0 between 600 and 800 hPa, due to the bigger q kernel K_q, has a much stronger impact on the WVF compared to the strong increase in q in MPI-ESM1-2-HR and ERA5 below 800 hPa.

Finally, the vertically resolved AF is considered (lower right panel). Analogously to the integrated values, the RH profile is a very good indicator for the AF profile. With the exception of MRI-ESM2-0, RH between about 900 and 600 hPa decreases (to different extents) for all analysed models. While RH in MRI-ESM2-0 does decrease between 600 and 700 hPa, it actually increases from 700 to 900 hPa. This is also reflected in the profile of AF, which can essentially be separated into two regimes: On one hand, there is the lower troposphere, where the dominating ATF leads to a net negative AF. On the other hand, the WVF dominates in the middle and upper troposphere leading to mostly positive AF. This separation is mainly due to the different peak heights of K_T and K_q, respectively. For MPI-ESM1-2-HR, CESM2-WACCM and ERA5, the transition between the two regimes occurs at around 600 hPa, with the overall shape of the feedback profiles looking very similar. For MRI-ESM2-0, however, the transition occurs much lower at around 800 hPa. This difference is not explained by the relatively similar kernels. Rather, almost all of the difference in AF between MRI-ESM2-0 and the other models originates in the lower troposphere between around 900 and 700 hPa, where RH increases in MRI-ESM2-0 but decreases in the other models.

In summary, the least negative λ_{AW} of MRI-ESM2-0 can be attributed to its close to zero AF, where due to its constant CRH with warming, ATF and WVF almost perfectly can-

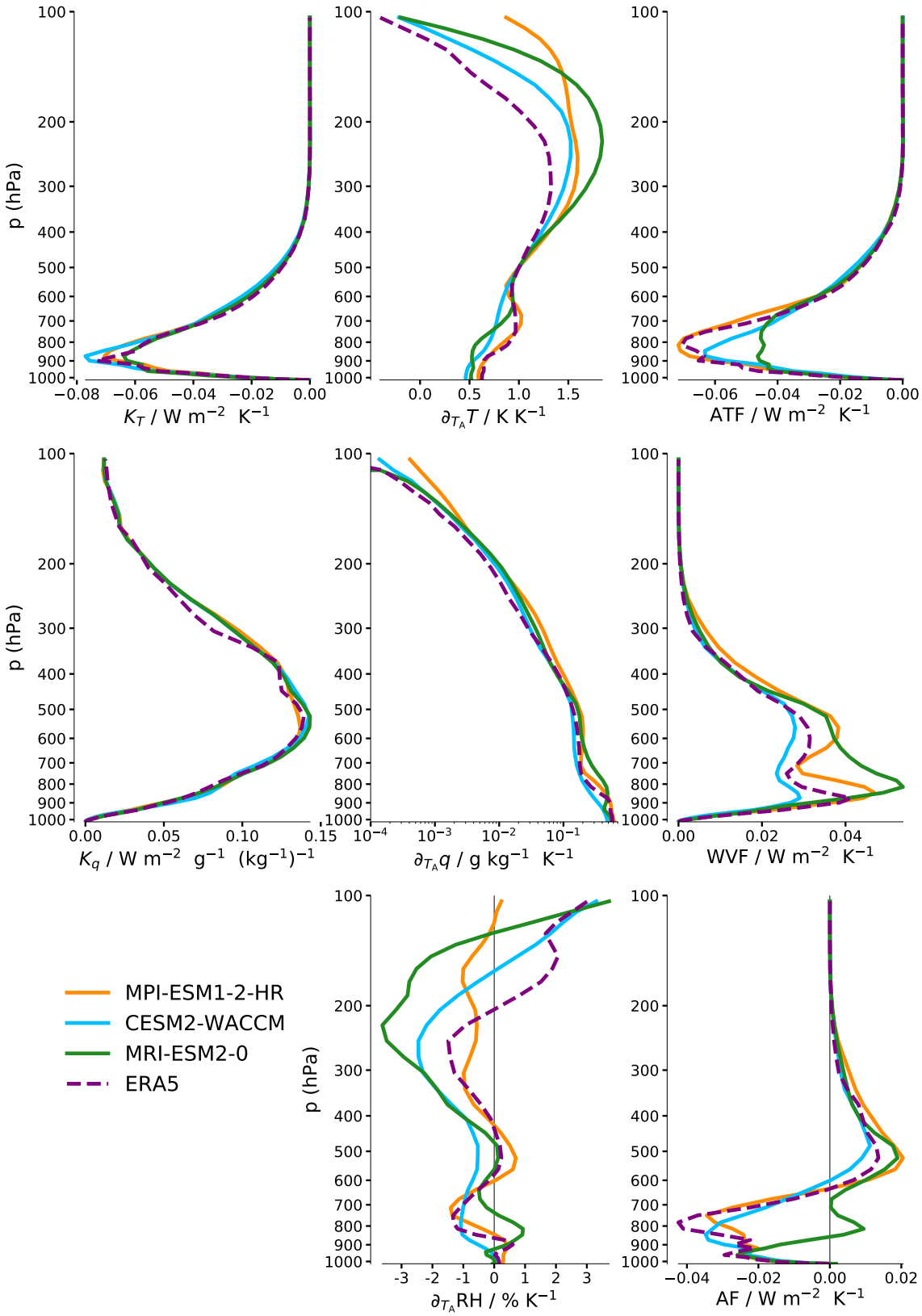

Figure 5.3: Vertically resolved atmospheric feedback kernels K_x, model responses $\partial_{T_A} x$ and climate feedbacks integrated over the atmospheric window: MPI-ESM1-2-HR (orange), CESM2-WACCM (blue), MRI-ESM2-0 (green) and ERA5 (dashed purple).

cel, whereas the other models analysed exhibit clearly negative ATF due to their CRH decreasing under warming. Most of the difference in RH change and therefore AF can be attributed to the layer between 900 and 700 hPa, where MRI-ESM2-0's RH is the only one showing an increase. This means that, if CRH stays constant under warming, the STF is the main factor determining λ_{AW}, as the atmospheric feedbacks cancel each other. Otherwise, the AF also has a significant impact.

In the following, the discrepancy in λ_{AW} between the CMIP6 models and the IASI observations is further analysed. Some of that difference can be reproduced applying the MSRK technique to ERA5. Its $\lambda_{\mathrm{AW,\,MSRK}}$ (-0.81 W m^{-2} K^{-1}) is more negative than the mean over the three CMIP6 models (-0.56 W m^{-2} K^{-1}), but less negative than IASI's λ_{AW} (-0.93 W m^{-2} K^{-1}) (Tab. 5.3). This difference in $\lambda_{\mathrm{AW,\,MSRK}}$ can in turn be traced back to two different causes. The first (and most obvious) is the inherently different representations of different feedback processes in ERA5 (and the real atmosphere) compared to CMIP6. This is mainly the case for the stronger STF caused by stronger surface warming $\partial_{T_{\mathrm{A}}}$SST and lower IWV in ERA5.

The second part is caused by biases due to the selection of analysed months (see Ch. 3). It can be quantified by also applying the MSRK method to the ERA5's mean quantities over a full ten year period (2010–2019) and comparing the results to those derived previously (where only the months, from which IASI observations are selected, are considered). The resulting $\lambda_{\mathrm{AW,\,MSRK}}$ is also shown in Tab. 5.3. $\lambda_{\mathrm{AW,\,MSRK}}$ for the full ten years is less negative than for the selected months, with a bias produced by the sub-sample selection of 0.08 W m^{-2} K^{-1}, overestimating the absolute value of $\lambda_{\mathrm{AW,\,MSRK}}$.

The sub-sample selection has no effect on the net atmospheric feedback (AF) (Tab. 5.5), as the absolute values of ATF and WVF are overestimated equally. In contrast, it substantially affects the surface temperature feedback (STF) (Tab. 5.6), mainly due to the significant overestimation of $\partial_{T_{\mathrm{A}}}$SST. The latter is much closer to the values of the CMIP6 models when the full ten years are considered. This overestimation seems to be mainly the result of only using data from four different years rather than using only six months per year (not shown). The bias in K_{SST} due to underestimating the IWV has only little impact.

This means that the difference in $\lambda_{\mathrm{AW,\,MSRK}}$ between ERA5 and CMIP6 (0.25 W m^{-2} K^{-1}) explains more than half of the difference in λ_{AW} between IASI and the CMIP6 mean (0.4 W m^{-2} K^{-1}). This difference in $\lambda_{\mathrm{AW,\,MSRK}}$ in turn is caused by inherently different atmospheric fields (0.17 W m^{-2} K^{-1}) and a bias due to the sub-sample selection (0.08 W m^{-2} K^{-1}). Accounting for those effects, this still leaves another 0.15 W m^{-2} K^{-1} to fully explain the different λ_{AW} of IASI and CMIP6. The remaining difference can be attributed to several factors.

Firstly, IASI's λ_{ν} is calculated from clear-sky pixels only. This is in contrast to CMIP6, where λ_{ν} is calculated from simulations of clear-sky spectra, which is accomplished by simply setting the cloud liquid water content to zero. All other variables are left un-

changed, most notably the specific humidity q. Filtering out only clear-sky pixels, as done for the IASI observations, however, also affects the mean humidity of the sampled profiles, introducing a clear-sky sampling dry bias (Allan et al., 2003; John et al., 2011). As demonstrated above, the strength of STF is enhanced for drier atmospheres.
Test runs, where the CMIP6 profiles are filtered based on their total cloud fraction (emulating the filtering applied to IASI), confirm the direction of the effect qualitatively. The λ_{AW} for the filtered profiles is more negative (due to the lower IWV), but the size of the effect strongly depends on the exact filtering methodology. Thus, the results are not robust enough to reliably quantify the strength of the clear-sky sampling bias. Furthermore, the different horizontal resolutions of the CMIP6 models (100 km or more) are an order of magnitude larger than IASI's minimal footprint of 12 km (see Ch. 3). This problem will only be resolved by future climate models with significantly higher horizontal resolution more comparable to that of IASI.
Lastly, even though it is strongly informed by observations, the T and q fields in ERA5 still differ from the actual atmospheric condition (Hersbach et al., 2020; Luo and Minnett, 2020). This means that while ERA5 profiles provide good approximations to the state of the real atmosphere observed by IASI, any comparison is inherently (at least somewhat) imprecise.
To conclude the analysis of λ_ν in the atmospheric window, the spectral shape of λ_ν is analysed briefly in the following. As the emission level shows little variation within the atmospheric window, being located mostly at or close to the surface (see Fig. 2.1), the focus in analysing λ_ν there mainly lies on analysing its integral over the whole band (λ_{AW}). Nevertheless, there are a few interesting features not captured by this approach. Note, that this analysis explicitly excludes the O_3 absorption band between 980 and 1080 cm^{-1}, which is separately discussed in Sec. 5.2.3. The analysis here (as the previous one concerning the integrated values) only discusses the atmospheric window within the spectral ranges defined in Tab. 2.1.
Apart from their different integrated values, the shapes of λ_ν differ between konrad and the other analysed models and instruments. λ_ν is relatively constant for the three CMIP6 models and for ERA5 within the atmospheric window. In contrast, konrad's λ_ν has a much "steeper" shape. Its absolute value reaches minima at the edges of the atmospheric window and its maximum at around 980 cm^{-1} (Fig. 5.4, left panel)[3]. This shape resembles that of the STF of the CMIP6 models (Fig. 5.4, right panel). As mentioned above, due to konrad's constant RH, its AF is zero in the atmospheric window. Not only is the band-integrated AF different from zero for most of the analysed models (as discussed above), it is especially negative at the edges of the atmospheric window at 1200 and at 800 cm^{-1} (Fig. 5.4, middle panel). This is even the case for MRI-ESM2-0, which exhibits all of its almost negligible AF in the atmospheric window towards the bands outer edges. This can

[3]The analysis is only shown for the λ_ν as inferred by the MSRK method in order to perform the feedback decomposition. Still, it applies analogously to the (very similar) λ_ν in the atmospheric window from (simulated) observations.

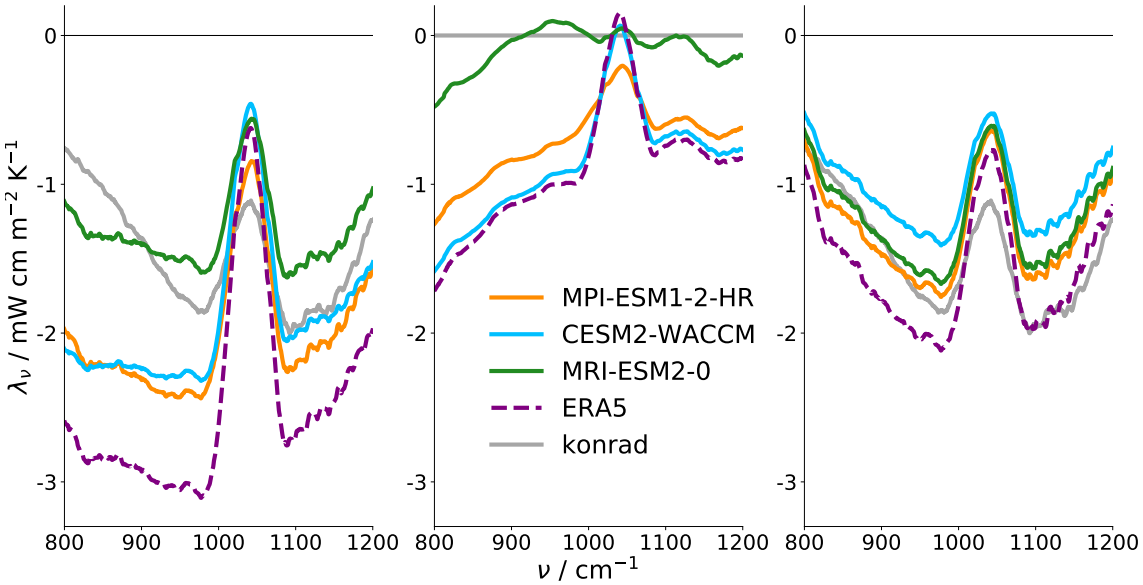

Figure 5.4: Total spectral feedback parameter in atmospheric window from mean spectral radiative kernel ($\lambda_{\nu,\,\mathrm{MSRK}}$) (left panel) and decomposed into spectral atmospheric temperature feedback (ATF_ν) (middle panel) and surface temperature feedback (STF_ν) (right panel).

be explained by the higher optical depth of the atmosphere there compared to the centre of the atmospheric window (Fig. 2.1). This leads to a smaller surface temperature kernel K_{SST} and stronger atmospheric kernels K_T and K_q (not shown), amplifying the effect of changes in the atmospheric T and q profiles, quantified by $\partial_{T_\mathrm{A}}\mathrm{CRH}$ (as described above). This feature counteracts the described effect of the STF, causing a much less "steep" shape of the overall λ_ν for the CMIP6 models and ERA5 compared to that of konrad.

5.2.2 Water vapour absorption bands

The H_2O bands in the mid-infrared (MIR) and far-infrared (FIR) are analysed together due to their very similar radiative properties (see Sec. 2.2). The λ_ν integrated over both bands (λ_{FIR} and λ_{MIR}, respectively) are shown in the first two columns of Tab. 5.7. As expected, they appear to be highly correlated, with λ_{FIR} being bigger by a factor of about two for all models. Similar to Sec. 5.2.1, the mean spectral radiative kernel (MSRK) technique is also employed (see Sec. 4.2). The λ_ν from that method integrated over both bands ($\lambda_{\mathrm{FIR,\,MSRK}}$ and $\lambda_{\mathrm{MIR,\,MSRK}}$) are shown for comparison in the last two columns of Tab. 5.7.

The values for MPI-ESM1-2-HR are near-zero for both H_2O bands, with the MSRK method producing more negative values by less than 0.02 W m^{-2} K^{-1}. On the other hand, CESM2-WACCM and MRI-ESM2-0 feature clear negative values in both H_2O bands, although the MSRK method delivers less negative values by up to 0.16 W m^{-2} K^{-1}. The λ_{MIR} ($\lambda_{\mathrm{MIR,\,MSRK}}$) inferred from IASI (ERA5), respectively, show very high agreement. They are more negative than those of MPI-ESM1-2-HR but not as negative as those of CESM2-

Table 5.7: Inferred λ_ν integrated over FIR (λ_{FIR}, $\lambda_{\text{FIR, MSRK}}$) and MIR ($\lambda_{\text{MIR}}$, $\lambda_{\text{MIR, MSRK}}$) using both (simulated) observations and MSRK methods. The CMIP6 mean refers to the mean over the three selected CMIP6 models.

	λ_{FIR} (W m^{-2} K^{-1})	λ_{MIR} (W m^{-2} K^{-1})	$\lambda_{\text{FIR, MSRK}}$ (W m^{-2} K^{-1})	$\lambda_{\text{MIR, MSRK}}$ (W m^{-2} K^{-1})
MPI-ESM1-2-HR	-0.08	-0.04	-0.09	-0.06
CESM2-WACCM	-0.49	-0.23	-0.33	-0.15
MRI-ESM2-0	-0.43	-0.19	-0.33	-0.14
CMIP6 mean	-0.33	-0.15	-0.25	-0.12
IASI	–	-0.10	–	–
ERA5 (selected months)	–	–	-0.14	-0.10
ERA5 (2010–2019)	–	–	-0.22	-0.12
konrad	-0.24	-0.12	–	–

WACCM and MRI-ESM2-0. This is also the case for ERA5's $\lambda_{\text{FIR, MSRK}}$ (due to its limited spectral coverage, there is no λ_{FIR} available for IASI). The mean over the analysed CMIP6 models shows that the MSRK method delivers about 20–25 % less negative values for both MIR and FIR. Nevertheless, even though they are not as similar as for the atmospheric window, both methods produce qualitatively similar results for both H_2O bands, allowing a feedback decomposition analogous to Sec. 5.2.1.

Analysing the decomposed feedbacks (Tab. 5.8 for the FIR and Tab. 5.9 for the MIR) confirms, as already discussed in Sec. 2.2, that the surface plays no role in determining λ_{FIR} and λ_{MIR} (the STF, shown in the first columns of both tables, is negligible). Hence, the total feedback is equal to the net atmospheric feedback (AF). It also reveals that the very negative λ_{MIR} and λ_{FIR} of MRI-ESM2-0 are caused by its strong atmospheric temperature feedback (ATF), compared to the other models. The very similar AF of CESM2-WACCM, however, is due to its comparatively weak water vapour feedback (WVF). Furthermore, the near-zero AF of MPI-ESM1-2-HR results from its very strong WVF almost balancing its ATF, which is still the second strongest among the models. Finally, ERA5 features the weakest ATF and second weakest WVF.

However, the data sub-sampling also seems to have an impact on the $\lambda_{\text{FIR, MSRK}}$ and $\lambda_{\text{MIR, MSRK}}$ as derived from ERA5 (as already discussed extensively in Sec. 5.2.1). For the full ten year period (2010–2019), ERA5's $\lambda_{\text{MIR, MSRK}}$ and especially $\lambda_{\text{FIR, MSRK}}$ are much more negative than when only 24 months are considered. The decomposition in Tab. 5.8 and Tab. 5.9 reveals that this discrepancy is largely due to the underestimation of ATF in the FIR and roughly equally caused by an underestimation of ATF and overestimation of WVF in the MIR.

The vertically resolved feedback kernels, model responses and feedbacks integrated over the FIR and MIR are shown in Fig. 5.5 and Fig. 5.6, respectively. Similar to the column-integrated values, the profiles also exhibit very similar behaviour. Apart from the larger absolute values in the FIR, two main differences stand out. Firstly, the profiles of the temperature kernels, and therefore also the ATF, span a greater vertical range in the FIR

.

Table 5.8: Column-integrated decomposed atmospheric feedbacks integrated over the FIR.

	STF (W m^{-2} K^{-1})	ATF (W m^{-2} K^{-1})	WVF (W m^{-2} K^{-1})	AF (W m^{-2} K^{-1})
MPI-ESM1-2-HR	-0.00	-1.51	1.41	-0.09
CESM2-WACCM	-0.00	-1.37	1.04	-0.33
MRI-ESM2-0	-0.00	-1.55	1.22	-0.33
ERA5 (selected months)	-0.00	-1.25	1.11	-0.14
ERA5 (2010–2019)	-0.00	-1.30	1.09	-0.22

.

Table 5.9: Column-integrated decomposed atmospheric feedbacks integrated over MIR.

	STF (W m^{-2} K^{-1})	ATF (W m^{-2} K^{-1})	WVF (W m^{-2} K^{-1})	AF (W m^{-2} K^{-1})
MPI-ESM1-2-HR	-0.00	-0.56	0.50	-0.06
CESM2-WACCM	-0.00	-0.52	0.37	-0.15
MRI-ESM2-0	-0.00	-0.58	0.43	-0.14
ERA5 (selected months)	-0.00	-0.50	0.41	-0.10
ERA5 (2010–2019)	-0.00	-0.52	0.39	-0.12

compared to the MIR. Secondly, the water vapour kernel assumes relatively higher values between 200 and 400 hPa in the MIR, which causes a higher part of the WVF to originate in that region. Those two effects combined also explain the different shapes of the net atmospheric feedback (AF) profiles, with less pronounced negative AF below 500 hPa and more pronounced positive AF above 300 hPa. However, in both spectral bands, both ATF and WVF mainly originate between 600 and 200 hPa, which is unsurprising given the high optical depth of both FIR and MIR, causing the emission level to lie in the middle to upper troposphere (Fig. 2.1). The following analysis (if not otherwise stated) is therefore valid for both H_2O bands.

The strong ATF of MPI-ESM1-2-HR and MRI-ESM2-0 result from their strong upper tropospheric warming above 400 hPa. The much less negative λ_{FIR} (and λ_{MIR}) of MPI-ESM1-2-HR compared to MRI-ESM2-0 mainly results from its stronger specific humidity response between about 200 and 400 hPa, causing a strong WVF in that layer.

As already seen in the atmospheric window, the change of relative humidity RH with the atmospheric temperature at 500 hPa T_{A} in a given atmospheric layer is a very good indicator for the AF originating from that layer (lower two panels). Most of the difference between the models featuring clearly negative λ_{FIR} and λ_{MIR} (CESM2-WACCM and MRI-ESM2-0) and those exhibiting less negative λ_{FIR} and λ_{MIR} (MPI-ESM1-2-HR and ERA5) mainly originates between 400 and 200 hPa due to the varying dependence of RH on T_{A} in those atmospheric layers, respectively. While MRI-ESM2-0 and CESM2-WACCM show quite strong decreases in RH, the decrease is much weaker for ERA5 and especially MPI-ESM1-2-HR.

Furthermore, the decreasing RH of CESM2-WACCM between 300 and 600 hPa is respon-

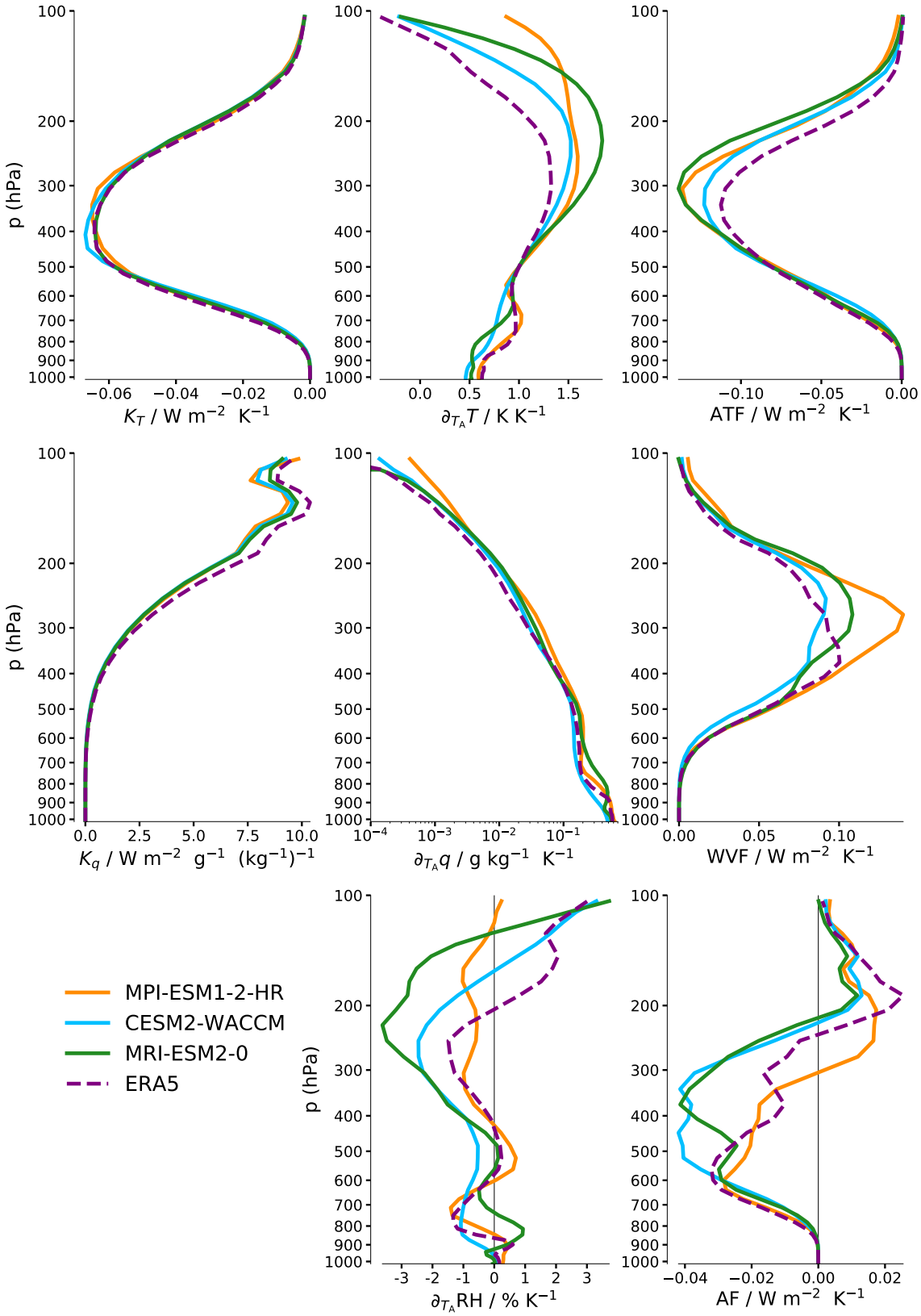

Figure 5.5: Vertically resolved atmospheric feedback kernels K_x, model responses $\partial_{T_A} x$ and climate feedbacks integrated over the FIR: MPI-ESM1-2-HR (orange), CESM2-WACCM (blue), MRI-ESM2-0 (green) and ERA5 (dashed purple).

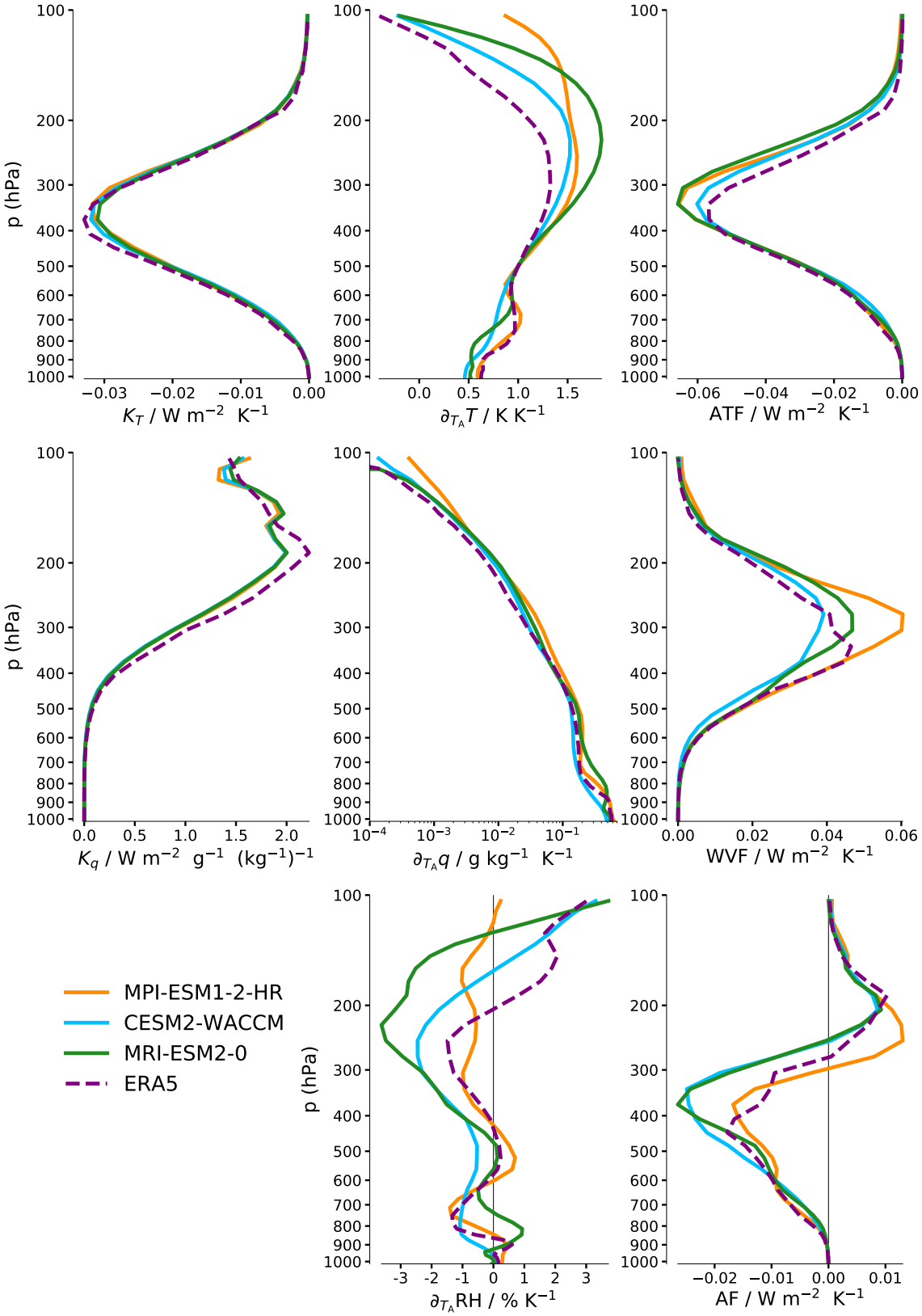

Figure 5.6: Vertically resolved atmospheric feedback kernels K_x, model responses $\partial_{T_A} x$ and climate feedbacks integrated over the MIR: MPI-ESM1-2-HR (orange), CESM2-WACCM (blue), MRI-ESM2-0 (green) and ERA5 (dashed purple).

sible for the strongly negative AF originating at those layers. Similarly, the quite strong positive AF of ERA5 above 200 hPa, is caused by its increase in RH in the tropopause region. This effect can mainly be seen in the FIR as that atmospheric region has only little impact in the MIR. Inversely, layers below 700 hPa (including the RH increase with T_A of MRI-ESM2-0, which strongly impacted λ_{AW}), have only minor impact on the overall λ_{FIR} and λ_{MIR}.

Due to the fact that the emission level varies significantly within both H_2O bands (see Sec. 2.2), the analysis is conducted beyond the band integrals. Additionally, the spectral shape of λ_ν in those bands is analysed more thoroughly. Using the emission level and emission range[4] for each wavenumber (upper right panel of Fig. 5.7), I link λ_ν to the change in RH at the respective atmospheric layer. The emission level and emission range rise from 500 ± 150 hPa for 550 cm^{-1} to 200 ± 50 hPa for 100 cm^{-1}, covering the middle and upper troposphere. To understand λ_ν at a certain wavenumber ν, one can follow a vertical line from the lower right to the upper right panel of Fig. 5.7 (as demonstrated by the vertical dashed black line) and then read of the changes in RH within the corresponding emission range shown in the upper left panel (dotted lines).

Several features in λ_ν can be explained this way. MPI-ESM1-2-HR's near-zero λ_ν for wavenumbers 100–450 cm^{-1} results from its almost constant RH with T_A at 150–400 hPa. In contrast, upper tropospheric RH decreases significantly in CESM2-WACCM and MRI-ESM2-0. The λ_ν reflect the spectral fingerprints of those changes of the RH profiles. For wavenumbers 100–350 cm^{-1}, which are mainly sensitive to RH changes at 150–400 hPa, MRI-ESM2-0 has the more negative λ_ν, consistent with its stronger RH decrease with T_A above 300 hPa. Analogously, CESM2-WACCM's λ_ν is more negative for wavenumbers 350–550 cm^{-1}, mainly sensitive to RH changes at 250–700 hPa, caused by its stronger RH decrease below 400 hPa. This behaviour is consistent with the theoretical framework of Simpson (1928a,b) and Ingram (2010) as well as the findings of Pan and Huang (2018), who already discussed the paramount importance of the change of RH under warming for (spectral) climate feedbacks.

For wavenumbers of 450–550 cm^{-1}, both MPI-ESM1-2-HR and CESM2-WACCM exhibit a strongly decreasing λ_ν with wavenumber, while λ_ν only moderately decreases for MRI-ESM2-0. Fig. 5.7 reveals that this spectral region (in contrast to smaller wavenumbers) is also sensitive to RH changes around 600–700 hPa, where RH decreases substantially for MPI-ESM1-2-HR and CESM2-WACCM but not for MRI-ESM2-0. This effect is additionally amplified by the increasing temperature dependence of the Planck curve at those wavenumbers.

Similar to the FIR, the emission level and emission range in the MIR also depend strongly on wavenumber. They rise from 600 ± 200 hPa at 1300 cm^{-1} to 300 ± 100 hPa at around

[4]The emission level is (as described above) determined as the height of the maximum of the temperature kernel (K_{T_i}), $K_{T_i,max}$ (due to the high optical depth, the contribution of the surface temperature kernel (K_{SST}) is negligible). The so-called emission range is here defined as the altitude range that substantially contributes to OLR_ν. This is quantified as layers where K_{T_i} is at least 50 % of $K_{T_i,max}$.

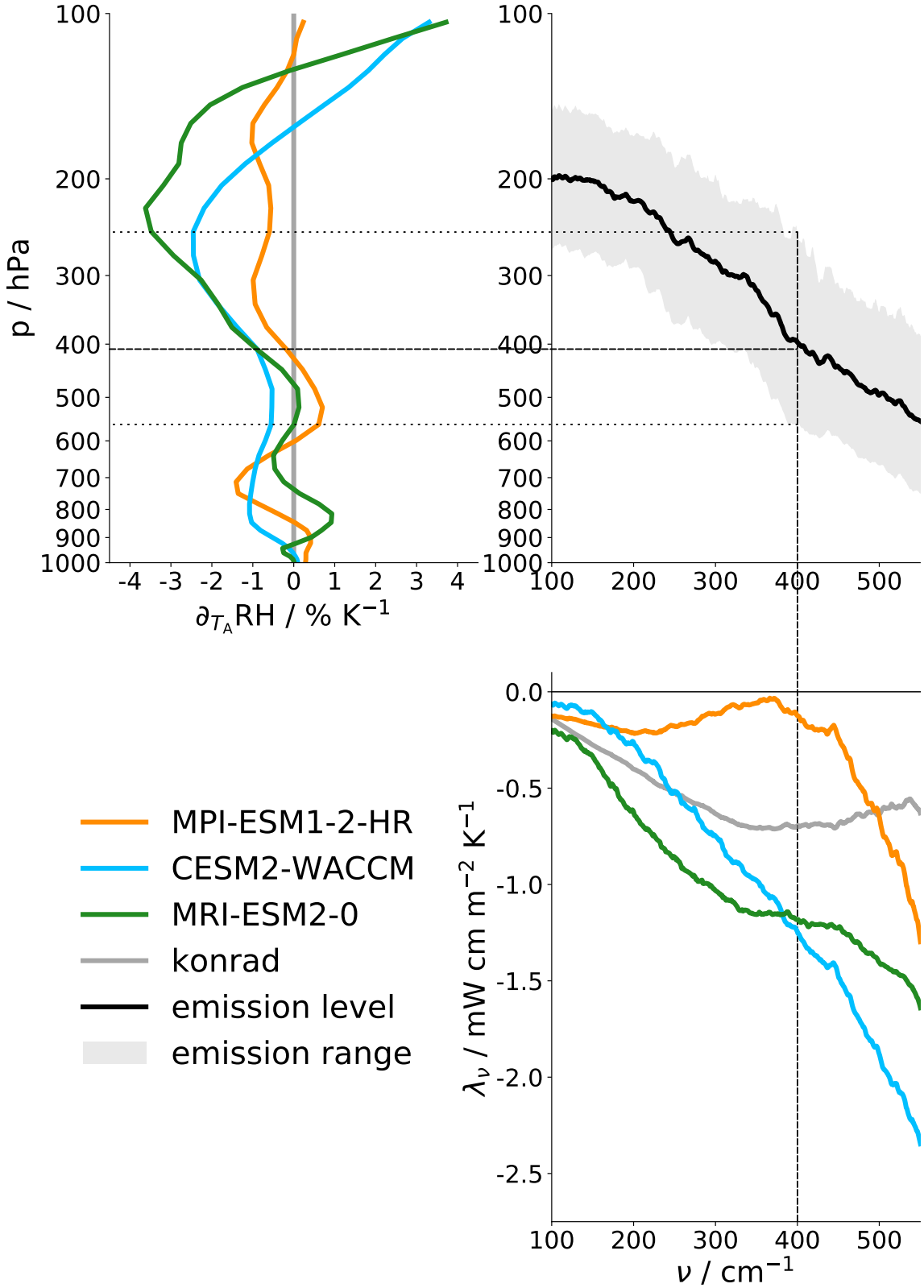

Figure 5.7: Spectral feedback parameter λ_ν in the FIR: MPI-ESM1-2-HR (orange), CESM2-WACCM (blue), MRI-ESM2-0 (green) and konrad (grey). (upper left) ∂_{T_A}RH (upper right): emission level (black line) and emission range (grey shading) (lower right): λ_ν in FIR. Both spectral plots show 50 cm^{-1} running means.

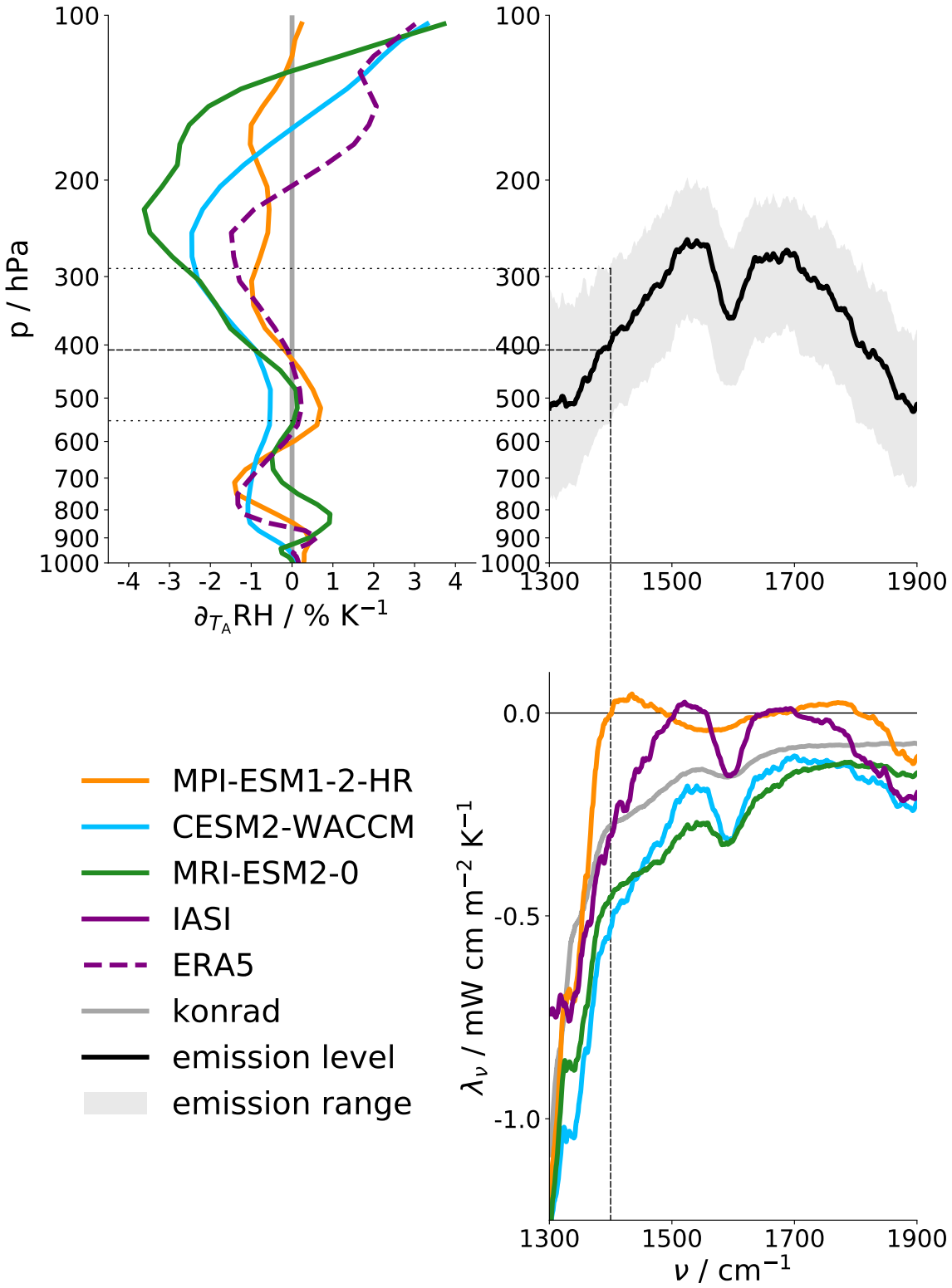

Figure 5.8: Spectral feedback parameter λ_ν in the MIR: MPI-ESM1-2-HR (orange), CESM2-WACCM (blue), MRI-ESM2-0 (green), IASI (solid purple), ERA5 (dashed purple) and konrad (grey). (upper left) ∂_{T_A}RH (upper right): emission level (black line) and emission range (grey shading) (lower right): λ_ν in FIR. Both spectral plots show 50 cm^{-1} running means.

1600 cm^{-1}, before sinking again to 600 $\pm$ 200 hPa at 1900 cm^{-1}. There are therefore many parallels, where λ_ν at certain wavenumbers in the FIR and MIR respectively are responsive to the same atmospheric layers (as already demonstrated in Fig. 2.1). In contrast to the FIR, the impact of the upper troposphere above 300 hPa is reduced in the MIR.
Despite those parallels between the two bands, a separate analysis of the MIR still has its merits. In contrast to the FIR, the MIR lies within the spectral range covered by IASI, allowing for comparison between observations and models. Fig. 5.8 is analogous to Fig. 5.7 but applied to the MIR spectral range, including λ_ν as inferred from IASI observations in the lower right panel and the average RH profile change for ERA5 in the upper left panel.
The change in ERA5's RH profile with warming (∂_{T_A}RH) explains large parts of the variations in IASI's λ_ν and how it compares to the λ_ν of the CMIP6 models. The IASI's λ_ν between around 1350 and 1850 cm^{-1} lies, for the most part, between that of MPI-ESM1-2-HR and those of the other two CMIP6 models. This is similar to ∂_{T_A}RH of ERA5 in the atmospheric layer to which λ_ν is mainly sensitive, namely between 600 and 200 hPa.
The emission level is the highest at around 1500 and 1700 cm^{-1}, respectively, where the H_2O absorption is the strongest. Around those wavenumbers, IASI's λ_ν matches or even slightly exceeds that of MPI-ESM1-2-HR, even reaching slightly positive values. This is consistent with the increase in RH in ERA5 above 200 hPa, which has substantial impact on λ_ν in those bands. In contrast, the CMIP6 models only feature increasing RH at even higher altitudes, which have an even smaller impact on their λ_ν. The only exception is CESM2-WACCM, which shows increasing RH above around 150 hPa and whose λ_ν surpasses MRI-ESM2-0's at around 1500 and 1700 cm^{-1}, respectively.
At the upper edge of the band at around 1900 cm^{-1}, IASI's λ_ν is closest to that of CESM2-WACCM, consistent with both models showing a decrease in RH below 600 hPa. Even though the emission level is similar at around 1300 cm^{-1}, IASI exhibits the least negative λ_ν. This probably has to do with the absorption bands of NH_4 and N_2O nearby and is not further discussed here.
Finally, λ_{MIR} as observed by IASI, combined with λ_{FIR} inferred from CMIP6 models can be used for a rough estimate of the λ_{FIR}, which in the future can be observed by the FORUM mission. For the three CMIP6 models analysed, λ_{FIR} is on average 2.13 times larger than λ_{MIR}. For λ_{MIR} of IASI of 0.10 W m^{-2} K^{-1}, this yields as an estimate of λ_{FIR} as observed by FORUM in the future of 0.20 W m^{-2} K^{-1} (both rounded). This is higher than ERA5's $\lambda_{\mathrm{FIR,\ MSRK}}$ of 0.14 W m^{-2} K^{-1}.
Spectrally resolved, λ_ν as observed by FORUM would likely be, following the relative magnitude of ERA5's ∂_{T_A}RH between 500 and 200 hPa, between that of MPI-ESM1-2-HR's and that of the other two models between 550 and roughly 250 cm^{-1}. Due to ERA5's increase in RH above 200 hPa, FORUM's λ_ν would probably be very close to zero (or even slightly positive) for smaller wavenumbers. This is somewhat similar to the spectral behaviour of λ_ν inferred from ERA5 using the MSRK method in the FIR (not shown).

All in all, λ_ν reflects the spectral fingerprint of changes in the atmospheric RH profile. The λ_ν at each wavenumber encompasses the effects of RH changes in a layer around the emission level. Similar to the atmospheric window, the sign of ∂_{T_A}RH strongly impacts that of the AF, underlying the paramount importance of understanding processes affecting how the profile of RH changes in a warming climate.

5.2.3 Ozone absorption band

The scope of this thesis is limited to spectral bands sensitive to changes in the troposphere (see Sec. 2.2). However, because of the striking difference in λ_ν between IASI and CMIP6 (which can be seen in Fig. 5.1 and the left panel of Fig. 5.4), the ozone (O_3) absorption band at 980–1080 cm^{-1} is briefly discussed in the following.
While λ_ν inferred from IASI is more negative in the O_3 band compared to the neighbouring atmospheric window, the opposite is the case for the λ_ν derived from models (CMIP6, ERA5 and konrad), whose absolute values of λ_ν decrease sharply. This is likely due to the fact that only climatological values of stratospheric O_3 are used for the radiative transfer simulations with RTTOV (see Sec. 4.1.1). Due to the high sensitivity of the results to the chosen assumptions, konrad omits ozone altogether (Lukas Kluft, personal communication). The apparent agreement of the different models in the ozone band should therefore be taken with a grain of salt.
Conversely, there are also a few factors possibly impacting IASI's behaviour in the ozone band. While it has the advantage of capturing the spectra produced by the actual O_3 concentration in the analysed years, the fact that only 24 months from four different years are selected reduces the robustness of the results (see Sec. 5.2.2). The regression standard error in the O_3 band is much larger compared to the atmospheric window, indicating that four yearly means might not be enough to accurately capture λ_ν there. On top of that, by selecting only a few years, effects like the quasi-biennial-oscillation (QBO)[5] might produce "artificial" correlations, which would not be encountered under forced warming. All in all, the methods available for this study do not allow any reliable conclusions about λ_ν between 980 and 1080 cm^{-1}.

[5]The QBO is a wave driven circulation with a period of around 30 months, dominating interannual variations in ozone concentration (Tung and Yang, 1994).

6 Conclusions and outlook

In this thesis, I develop a new method for inferring the longwave spectral climate feedback parameter λ_ν from interannual variations of the spectral outgoing longwave radiation $\mathrm{OLR}_\nu$and the atmospheric temperature at 500 hPa T_A for clear-skies over the tropical ocean. The inferred broadband values for λ are consistent with results of other methods when applied to the same domain (Gregory et al., 2004).
The feedbacks making up λ_ν are linearly decomposed using mean spectral radiative kernels (MSRKs), following the approaches of Held and Soden (2006), Soden et al. (2008) and Huang et al. (2014). This decomposition into surface temperature feedback (STF), atmospheric temperature feedback (ATF) and water vapour feedback (WVF) is found to be in good agreement with the λ_ν described above.
The STF makes up the largest part of the λ_ν integrated over the atmospheric window (λ_AW). It is proportional to the warming of sea surface temperature (SST) with T_A ($\partial_{T_\mathrm{A}}\mathrm{SST}$). Models with higher integrated water vapour IWV feature weaker STF, as parts of the surface signal is masked by H_2O continuum absorption. For near-constant column relative humidity CRH with warming ($\partial_{T_\mathrm{A}}\mathrm{CRH} \approx 0$) (which is only the case for MRI-ESM2-0), the contribution of the net atmospheric feedback (AF) is negligible, as ATF and WVF almost perfectly cancel. Most models (MPI-ESM1-2-HR, CESM2-WACCM, ERA5), however, exhibit negative $\partial_{T_\mathrm{A}}\mathrm{CRH}$, causing a negative AF of similar magnitude as STF.
The λ_AW inferred from IASI observations is more negative compared to the CMIP6 models. This is found to be due to a combination of several effects. Calculating MSRKs for ERA5, it is found that the average IWV is lower than in the CMIP6 models. ERA5 also features a stronger surface warming, which is mainly due to a bias caused by the subsampling of the data. Finally, a clear-sky sampling dry bias (Allan et al., 2003; John et al., 2011) likely also contributes.
In the H_2O bands in the mid-infrared (MIR) and far-infrared (FIR), λ_ν is only impacted by atmospheric feedbacks, as the surface plays no role due to the high optical depth τ. The mean RH change in the layer around the emission level is found to be a very good indicator for λ_ν in those bands. Two of the models (MRI-ESM2-0 and CESM2-WACCM) exhibit strong decreases in RH in the upper troposphere causing strongly negative λ_ν in both H_2O bands. On the other hand, ERA5 and especially MPI-ESM1-2-HR have closer to zero upper tropospheric $\partial_{T_\mathrm{A}}\mathrm{RH}$ and hence also less negative λ_ν.
The importance of changes in RH with warming has been found for ECS (and therefore λ) in general (Bourdin et al., 2021) and for the OLR in the H_2O bands in particular (Simpson, 1928a; Ingram, 2010). This work highlights the importance of changes in RH for λ_ν

in the H_2O bands, but also in the atmospheric window (AW).

The largest inter-model difference in λ_ν in this study occurs in the FIR, with λ_{FIR} ranging from near-zero to a substantial negative contribution. This uncertainty is magnified due to the large temperature dependence of the Planck curve in the FIR between 400 and 550 cm^{-1}. However, as previously mentioned, there are currently no hyperspectral satellite observations for wavenumbers below 645 cm^{-1}. This will be changed by the Far-infrared-Outgoing-Radiation Understanding and Monitoring (FORUM) mission which is currently in planning. Flying in tandem with IASI-NG, FORUM will for the first time provide hyperspectral observations of almost the whole spectral range of significant OLR_ν (Domínguez et al., 2020). This will help to improve our understanding of the governing feedback processes in this vital spectral region and enabling the inference of the full longwave λ_ν based on satellite observations.

The fact that all CMIP6 models and ERA5 show at least some decrease in CRH with warming is a somewhat unexpected result. While the decrease of RH in the upper tropical troposphere found in this thesis is consistent with previous studies of global climate models, this is not the case for the lower and middle tropical troposphere, where RH is found to be constant or even increase (Sherwood et al., 2010). The majority of the models analysed in this study (MPI-ESM1-2-HR, CESM2-WACCM and ERA5, but not MRI-ESM2-0), however, feature a decrease in RH below 600 hPa, which is also the main cause for their decreasing CRH with T_A. This lower tropospheric RH decrease has also been found by Bourdin et al. (2021), who investigated RH trends in the ERA5 and JRA-55 reanalyses over 40 years. But they also found increasing RH in the mid- and upper troposphere (above 600 hPa), contrary to the findings in this study, which only finds increasing RH above 200 hPa in ERA5 for both the sub-sampled months and the full ten year period from 2010 to 2019.

It would be interesting to investigate, whether the decrease in lower and middle tropospheric RH (and therefore the CRH) found in this study is merely a feature of interannual variability or the selected set of models, or if it can be reproduced under forced warming for a larger model ensemble (e. g., using the 4xCO2 experiment). If that is the case, this would be a significant result, possibly indicating an additional stabilising feedback delaying the closing of the atmospheric window, akin to the controversial iris-hypothesis introduced by Lindzen et al. (2001).

The results from this thesis are also consistent with the findings of John and Soden (2007), who found that the water vapour feedback (WVF) and lapse rate feedback (LRF) depend relatively little on the model mean state but rather on their responses to surface warming. This has also been found in this thesis, where parameters like the mean IWV have a smaller impact (even in the atmospheric window, AW) than the models responses like the changes of SST and CRH with T_A. Contrary to the findings of John and Soden (2007), the model responses are found to vary substantially and in turn to be largely responsible for inter-model differences in λ_ν in this study. It would be intriguing to explore how these

differences depend on the selection of models and experiments, but also on the analysed domains and time periods as well as on which atmospheric temperature is used as a reference for the regression.

For future studies, it would make sense to extend the amount of IASI data used to avoid biases that arise from only selecting a sub-sample (e. g., ten full years, as done for the CMIP6 models). One could also increase the robustness of the regression by using monthly deviations from the mean annual cycle of OLR_ν and T_A instead of yearly means, increasing the number of data points based on which the regression is performed. While this is not expected to substantially change the outcome, it would relate to another possible adjustment of the inference method. Contrary to Dessler and Forster (2018), the time series of OLR_ν and T_A are not detrended in this study, as the spectral decomposition relies much more on a maximised signal-to-noise ratio, which is reduced by the detrending. But it might be suitable to apply to a more robust regression.

Further investigations could also rely more on the mean spectral radiative kernel (MSRK) method, calculating the kernels with high temporal and spatial resolution, instead of only calculating them for the mean state. This approach would be similar to that of Huang et al. (2014), but for short-term variability instead of forced model runs, also allowing conclusions about how the results of those two approaches compare spectrally. The spectral radiative kernel method could even be applied to IASI observations by using retrieved temperature and humidity profiles (Carissimo et al., 2005).

This study demonstrates that it is possible to infer λ_ν from hyperspectral satellite observations of interannual variability. The differences between the λ_ν inferred from different CMIP6 models as well as the IASI observations can be understood by decomposing λ_ν into its main feedbacks using MSRKs. Analysing different parts of the spectrum separately gives valuable insights into inter-model differences in λ_ν that compensate in the total λ. For example, while MPI-ESM1-2-HR and MRI-ESM2-0 have rather similar overall λ (-1.43 and -1.62 W m^{-2} K^{-1}, respectively), the former has a significantly more stabilising feedbacks in the atmospheric window, while the latter features a much larger contributions of the H_2O bands. As those bands are mainly sensitive to the surface and upper troposphere, respectively, the dominating feedbacks are driven by different processes that might respond differently to future warming. Hence, a better understanding of those processes and how they affect λ_ν are of paramount value to climate research.

Acknowledgements

Firstly, I want to thank my primary supervisor, Stefan Buehler, for guiding me through the project and helping me develop the key scientific questions, while still allowing for this thesis to be my own work.
I am also very thankful to my secondary supervisor, Manfred Brath, for a lot of long discussions, for suggesting new ideas when I got stuck, and for answering many questions I had throughout my work.
In this context I also want to thank Lukas Kluft, for giving valuable input at many different points throughout my work on this thesis, as well as for performing model simulations providing reference values for the analysis.
A special thank you also goes to Viju John, for participating in several discussions, and for transferring the large amount of IASI data, which would have been impractical otherwise.
Finally, I want to thank Oliver Lemke, for always patiently giving support with all sorts of technical problems I encountered during my work, and also for assisting in the transfer of the IASI data.

List of Figures

List of Tables

Bibliography

Allan, R. P., M. A. Ringer, and A. Slingo (2003). "Evaluation of moisture in the Hadley Centre climate model using simulations of HIRS water-vapour channel radiances". In: *Quarterly Journal of the Royal Meteorological Society* 129.595, pp. 3371–3389. DOI: 10.1256/qj.02.217.

Allen, M. R. and W. J. Ingram (2002). "Constraints on future changes in climate and the hydrologic cycle". In: *Nature* 419, pp. 224–232. DOI: 10.1038/nature01092.

August, T., D. Klaes, P. Schlüssel, T. Hultberg, M. Crapeau, A. Arriaga, A. O'Carroll, D. Coppens, R. Munro, and X. Calbet (2012). "IASI on Metop-A: Operational Level 2 retrievals after five years in orbit". In: *Journal of Quantitative Spectroscopy and Radiative Transfer* 113.11. Three Leaders in Spectroscopy, pp. 1340–1371. ISSN: 0022-4073. DOI: 10.1016/j.jqsrt.2012.02.028.

Blumstein, D., G. Chalon, T. Carlier, C. Buil, P. Hébert, T. Maciaszek, G. Ponce, T. Phulpin, B. Tournier, D. Simeoni, P. Astruc, and A. Clauss (Nov. 2004). "IASI instrument: Technical overview and measured performances". In: *Proceedings of SPIE - The International Society for Optical Engineering* 5543. DOI: 10.1117/12.560907.

Bouillon, M., S. Safieddine, J. Hadji-Lazaro, S. Whitburn, L. Clarisse, M. Doutriaux-Boucher, D. Coppens, T. August, E. Jacquette, and C. Clerbaux (2020). "Ten-year assessment of IASI radiance and temperature". In: *Remote Sensing* 12.15, p. 2393. DOI: 10.3390/rs12152393.

Bourdin, S., L. Kluft, and B. Stevens (2021). "Dependence of Climate Sensitivity on the Given Distribution of Relative Humidity". In: *Geophysical Research Letters* 48.8, e2021GL–092462. DOI: 10.1029/2021GL092462.

Buehler, S. A., J. Mendrok, P. Eriksson, A. Perrin, R. Larsson, and O. Lemke (2018). "ARTS, the Atmospheric Radiative Transfer Simulator – version 2.2, the planetary toolbox edition". In: *Geoscientific Model Development* 11.4, pp. 1537–1556. DOI: 10.5194/gmd-11-1537-2018.

Carissimo, A., I. De Feis, and C. Serio (2005). "The physical retrieval methodology for IASI: the δ-IASI code". In: *Environmental Modelling & Software* 20.9, pp. 1111–1126. ISSN: 1364-8152. DOI: 10.1016/j.envsoft.2004.07.003.

Clerbaux, N., S. Dewitte, L. Gonzalez, C. Bertrand, B. Nicula, and A. Ipe (2003). "Outgoing longwave flux estimation: improvement of angular modelling using spectral information". In: *Remote Sensing of Environment* 85.3, pp. 389–395. ISSN: 0034-4257. DOI: 10.1016/S0034-4257(03)00015-4.

Dacie, S., L. Kluft, H. Schmidt, B. Stevens, S. A. Buehler, P. J. Nowack, S. Dietm?ller, N. L. Abraham, and T. Birner (2019). "A 1D RCE Study of Factors Affecting the Tropical Tropopause Layer and Surface Climate". In: *Journal of Climate* 32.20, pp. 6769–6782. DOI: 10.1175/JCLI-D-18-0778.1.

Danabasoglu, G. and P. R. Gent (2009). "Equilibrium Climate Sensitivity: Is It Accurate to Use a Slab Ocean Model?" In: *Journal of Climate* 22.9, pp. 2494–2499. DOI: 10.1175/2008JCLI2596.1.

Dessler, A. E. (2013). "Observations of Climate Feedbacks over 2000–10 and Comparisons to Climate Models". In: *Journal of Climate* 26.1, pp. 333–342. DOI: 10.1175/JCLI-D-11-00640.1.

Dessler, A. E. and P. M. Forster (2018). "An Estimate of Equilibrium Climate Sensitivity From Interannual Variability". In: *Journal of Geophysical Research: Atmospheres* 123.16, pp. 8634–8645. DOI: 10.1029/2018JD028481.

Dessler, A. E., T. Mauritsen, and B. Stevens (2018). "The influence of internal variability on Earth's energy balance framework and implications for estimating climate sensitivity". In: *Atmospheric Chemistry and Physics* 18.7, pp. 5147–5155. DOI: 10.5194/acp-18-5147-2018.

Domínguez, B. C., C. Pachot, H. Oetjen, F. Mariani, S. Riel, A. Tromba, D. Lajas, D. Schuettemeyer, B. Sierk, N. Leveque, M.-G. Kolm, H. Korswagen, and W. Posselt (2020). "The Far-Infrared Outgoing Radiation Understanding and Monitoring (Forum) Mission. ESA's 9th Earth Explorer". In: *IGARSS 2020 - 2020 IEEE International Geoscience and Remote Sensing Symposium*, pp. 6035–6038. DOI: 10.1109/IGARSS39084.2020.9323185.

Eriksson, P., S. Buehler, C. Davis, C. Emde, and O. Lemke (2011). "ARTS, the atmospheric radiative transfer simulator, version 2". In: *Journal of Quantitative Spectroscopy and Radiative Transfer* 112.10, pp. 1551–1558. ISSN: 0022-4073. DOI: 10.1016/j.jqsrt.2011.03.001.

EUMETSAT (2018). *IASI Level 1C Climate Data Record Release 1 - Metop-A*. European Organisation for the Exploitation of Meteorological Satellites. DOI: 10.15770/EUM_SEC_CLM_0014.

Eyring, V., S. Bony, G. A. Meehl, C. A. Senior, B. Stevens, R. J. Stouffer, and K. E. Taylor (2016). "Overview of the Coupled Model Intercomparison Project Phase 6 (CMIP6) experimental design and organization". In: *Geoscientific Model Development* 9.5, pp. 1937–1958. DOI: 10.5194/gmd-9-1937-2016.

Feldl, N. and G. H. Roe (2013). "Four perspectives on climate feedbacks". In: *Geophysical Research Letters* 40.15, pp. 4007–4011. DOI: 10.1002/grl.50711.

Friedrich, T. and A. Timmermann (2020). "Using Late Pleistocene sea surface temperature reconstructions to constrain future greenhouse warming". In: *Earth and Planetary Science Letters* 530, p. 115911. ISSN: 0012-821X. DOI: 10.1016/j.epsl.2019.115911.

Gregory, J. M., W. J. Ingram, M. A. Palmer, G. S. Jones, P. A. Stott, R. B. Thorpe, J. A. Lowe, T. C. Johns, and K. D. Williams (2004). "A new method for diagnosing radiative forcing and climate sensitivity". In: *Geophysical Research Letters* 31.3. DOI: 10.1029/2003GL018747.

Hansen, J., A. Lacis, D. Rind, G. Russell, P. Stone, I. Fung, R. Ruedy, and J. Lerner (1984). "Climate sensitivity: Analysis of feedback mechanisms". In: *Climate Processes and Climate Sensitivity*. Ed. by J. E. Hansen and T. Takahashi. AGU Geophysical Monograph 29, Maurice Ewing Vol. 5. Washington, D.C.: American Geophysical Union, pp. 130–163.

Harris, C. R., K. J. Millman, S. J. van der Walt, R. Gommers, P. Virtanen, D. Cournapeau, E. Wieser, J. Taylor, S. Berg, N. J. Smith, R. Kern, M. Picus, S. Hoyer, M. H. van Kerkwijk, M. Brett, A. Haldane, J. F. del Río, M. Wiebe, P. Peterson, P. Gérard-Marchant, K. Sheppard, T. Reddy, W. Weckesser, H. Abbasi, C. Gohlke, and T. E. Oliphant (Sept. 2020). "Array programming with NumPy". In: *Nature* 585.7825, pp. 357–362. DOI: 10.1038/s41586-020-2649-2.

Held, I. M. and K. M. Shell (2012). "Using Relative Humidity as a State Variable in Climate Feedback Analysis." In: *Journal of Climate* 25.8, pp. 2578–2582. DOI: 10.1175/JCLI-D-11-00721.1.

Held, I. M. and B. J. Soden (2006). "An Assessment of Climate Feedbacks in Coupled Ocean–Atmosphere Models". In: *Journal of Climate* 19.14, pp. 3354–3360. DOI: 10.1175/JCLI3799.1.

Hersbach, H., B. Bell, P. Berrisford, G. Biavati, A. Horányi, J. Muñoz Sabater, J. Nicolas, C. Peubey, R. Radu, I. Rozum, D. Schepers, A. Simmons, C. Soci, D. Dee, and J.-N. Thépaut (2019a). *ERA5 monthly averaged data on single levels from 1979 to present*. Copernicus Climate Change Service (C3S) Climate Data Store (CDS). (Accessed on 26-01-2021). DOI: 10.24381/cds.f17050d7.

– (2019b). *ERA5 monthly averaged data on pressure levels from 1979 to present*. Copernicus Climate Change Service (C3S) Climate Data Store (CDS). (Accessed on 02-06-2021). DOI: 10.24381/cds.6860a573.

Hersbach, H., B. Bell, P. Berrisford, S. Hirahara, A. Horányi, J. Muñoz-Sabater, J. Nicolas, C. Peubey, R. Radu, D. Schepers, A. Simmons, C. Soci, S. Abdalla, X. Abellan, G. Balsamo, P. Bechtold, G. Biavati, J. Bidlot, M. Bonavita, G. De Chiara, P. Dahlgren, D. Dee, M. Diamantakis, R. Dragani, J. Flemming, R. Forbes, M. Fuentes, A. Geer, L. Haimberger, S. Healy, R. J. Hogan, E. Hólm, M. Janisková, S. Keeley, P. Laloyaux, P. Lopez, C. Lupu, G. Radnoti, P. de Rosnay, I. Rozum, F. Vamborg, S. Villaume, and J.-N. Thépaut (2020). "The ERA5 global reanalysis". In: *Quarterly Journal of the Royal Meteorological Society* 146.730, pp. 1999–2049. DOI: 10.1002/qj.3803.

Hocking, J., P. Rayer, D. Rundle, R. Saunders, M. Matricardi, A. Geer, P. Brunel, and J. Vidot (2019). *RTTOV v12 Users Guide*. NWP SAF. URL: https://nwp-saf.eumetsat.

int/site/download/documentation/rtm/docs_rttov12/users_guide_rttov12_v1.3.pdf.

Huang, X., X. Chen, B. J. Soden, and X. Liu (2014). "The spectral dimension of longwave feedback in the CMIP3 and CMIP5 experiments". In: *Geophysical Research Letters* 41.22, pp. 7830–7837. DOI: 10.1002/2014GL061938.

Illingworth, S. M., J. J. Remedios, and R. J. Parker (2009). "Intercomparison of integrated IASI and AATSR calibrated radiances at 11 and 12 μm". In: *Atmospheric Chemistry and Physics* 9.18, pp. 6677–6683. DOI: 10.5194/acp-9-6677-2009.

Ingram, W. J. (2002). "On the Robustness of the Water Vapor Feedback: GCM Vertical Resolution and Formulation". In: *Journal of Climate* 15.9, pp. 917–921. DOI: 10.1175/1520-0442(2002)015<0917:OTROTW>2.0.CO;2.

– (2010). "A very simple model for the water vapour feedback on climate change". In: *Quarterly Journal of the Royal Meteorological Society* 136.646, pp. 30–40. DOI: 10.1002/qj.546.

John, V. O. and B. J. Soden (2007). "Temperature and humidity biases in global climate models and their impact on climate feedbacks". In: *Geophysical Research Letters* 34.18. DOI: 10.1029/2007GL030429.

John, V. O., G. Holl, R. P. Allan, S. A. Buehler, D. E. Parker, and B. J. Soden (2011). "Clear-sky biases in satellite infrared estimates of upper tropospheric humidity and its trends". In: *Journal of Geophysical Research: Atmospheres* 116.D14. DOI: 10.1029/2010JD015355.

Kato, S. and N. G. Loeb (2005). "Top-of-atmosphere shortwave broadband observed radiance and estimated irradiance over polar regions from Clouds and the Earth's Radiant Energy System (CERES) instruments on Terra". In: *Journal of Geophysical Research: Atmospheres* 110.D7. DOI: 10.1029/2004JD005308.

Keil, P., H. Schmidt, and B. Stevens (2020). "Lapse rate deviations from the moist adiabat in the tropical upper troposphere in climate models". In: *EGU General Assembly 2020* Online, 4–8 May 2020.EGU2020-9467. DOI: 10.5194/egusphere-egu2020-9467.

Klaes, K. D., M. Cohen, Y. Buhler, P. Schlüssel, R. Munro, J.-P. Luntama, A. von Engeln, E. Ó. Clérigh, H. Bonekamp, J. Ackermann, and J. Schmetz (2007). "An Introduction to the EUMETSAT Polar system". In: *Bulletin of the American Meteorological Society* 88.7, pp. 1085–1096. DOI: 10.1175/BAMS-88-7-1085.

Kluft, L. and S. Dacie (2021). *atmtools/konrad: A radiative-convective equilibrium model for Python*. DOI: 10.5281/zenodo.4434837.

Kluft, L., S. Dacie, S. A. Buehler, H. Schmidt, and B. Stevens (2019). "Re-Examining the First Climate Models: Climate Sensitivity of a Modern Radiative-Convective Equilibrium Model". In: *Journal of Climate* 32.23, pp. 8111–8125. DOI: 10.1175/JCLI-D-18-0774.1.

Koll, D. D. B. and T. W. Cronin (2018). "Earth's outgoing longwave radiation linear due to H2O greenhouse effect". In: *Proceedings of the National Academy of Sciences* 115.41, pp. 10293–10298. ISSN: 0027-8424. DOI: 10.1073/pnas.1809868115.

Kythe, P. and P. Puri (2011). *Computational methods for linear integral equations*. Springer Science & Business Media.

Larar, A. M., W. L. Smith, D. K. Zhou, X. Liu, H. Revercomb, J. P. Taylor, S. M. Newman, and P. Schlüssel (2010). "IASI spectral radiance validation inter-comparisons: case study assessment from the JAIVEx field campaign". In: *Atmospheric Chemistry and Physics* 10.2, pp. 411–430. DOI: 10.5194/acp-10-411-2010.

Li, J. and H. W. Barker (2018). "Computation of domain-average radiative flux profiles using Gaussian quadrature". In: *Quarterly Journal of the Royal Meteorological Society* 144.712, pp. 720–734. DOI: 10.1002/qj.3241.

Liang, S. and A. Strahler (1993). "Calculation of the angular radiance distribution for a coupled atmosphere and canopy". In: *IEEE Transactions on Geoscience and Remote Sensing* 31.2, pp. 491–502. DOI: 10.1109/36.214925.

Lindzen, R. S., M.-D. Chou, and A. Y. Hou (2001). "Does the Earth Have an Adaptive Infrared Iris?" In: *Bulletin of the American Meteorological Society* 82.3, pp. 417–432. DOI: 10.1175/1520-0477(2001)082<0417:DTEHAA>2.3.CO;2.

Liou, K. (2002). *An introduction to atmospheric radiation*. 2nd Edition. San Diego, CA: Academic Press.

Loeb, N. G., S. Kato, K. Loukachine, and N. Manalo-Smith (2005). "Angular Distribution Models for Top-of-Atmosphere Radiative Flux Estimation from the Clouds and the Earth's Radiant Energy System Instrument on the Terra Satellite. Part I: Methodology". In: *Journal of Atmospheric and Oceanic Technology* 22.4, pp. 338–351. DOI: 10.1175/JTECH1712.1.

Luo, B. and P. J. Minnett (2020). "Evaluation of the ERA5 Sea Surface Skin Temperature with Remotely-Sensed Shipborne Marine-Atmospheric Emitted Radiance Interferometer Data". In: *Remote Sensing* 12.11. ISSN: 2072-4292. DOI: 10.3390/rs12111873.

Maycock, A. C. (2016). "The contribution of ozone to future stratospheric temperature trends". In: *Geophysical Research Letters* 43.9, pp. 4609–4616. DOI: 10.1002/2016GL068511.

Meehl, G. A. and W. M. Washington (1996). "El Niño-like climate change in a model with increased atmospheric CO_2 concentrations". In: *Nature* 382.6586, pp. 56–60. DOI: 10.1038/382056a0.

Meng, X., H. Li, Y. Du, Q. Liu, J. Zhu, and L. Sun (2016). "Retrieving land surface temperature from Landsat 8 TIRS data using RTTOV and ASTER GED". In: *2016 IEEE International Geoscience and Remote Sensing Symposium (IGARSS)*, pp. 4302–4305. DOI: 10.1109/IGARSS.2016.7730121.

Pan, F. and X. Huang (2018). "The Spectral Dimension of Modeled Relative Humidity Feedbacks in the CMIP5 Experiments". In: *Journal of Climate* 31.24, pp. 10021–10038. DOI: 10.1175/JCLI-D-17-0491.1.

Pavelin, E. G., S. J. English, and J. R. Eyre (2008). "The assimilation of cloud-affected infrared satellite radiances for numerical weather prediction". In: *Quarterly Journal of the Royal Meteorological Society* 134.632, pp. 737–749. DOI: 10.1002/qj.243.

Pendergrass, A. G., A. Conley, and F. M. Vitt (2018). "Surface and top-of-atmosphere radiative feedback kernels for CESM-CAM5". In: *Earth System Science Data* 10.1, pp. 317–324. DOI: 10.5194/essd-10-317-2018.

Proistosescu, C., A. Donohoe, K. C. Armour, G. H. Roe, M. F. Stuecker, and C. M. Bitz (2018). "Radiative Feedbacks From Stochastic Variability in Surface Temperature and Radiative Imbalance". In: *Geophysical Research Letters* 45.10, pp. 5082–5094. DOI: 10.1029/2018GL077678.

Righetti, P., J. de Juana Gamo, and F. Sancho (2020). "Metop-C deployment and start of three-satellite operations". In: *The Aeronautical Journal* 124.1276, pp. 902–916. DOI: 10.1017/aer.2020.10.

Roe, G. H. and K. C. Armour (2011). "How sensitive is climate sensitivity?" In: *Geophysical Research Letters* 38.14. DOI: 10.1029/2011GL047913.

Rushley, S. S., D. Kim, C. S. Bretherton, and M.-S. Ahn (2017). "Reexamining the Nonlinear Moisture-Precipitation Relationship Over the Tropical Oceans". In: *Geophysical Research Letters* 45.2, pp. 1133–1140. DOI: 10.1002/2017GL076296.

Sanderson, B., K. Shell, and W. Ingram (2010). "Climate feedbacks determined using radiative kernels in a multi-thousand member ensemble of AOGCMs". In: *Clim Dyn* 35, pp. 1219–1236. DOI: 10.1007/s00382-009-0661-1.

Saunders, R., J. Hocking, E. Turner, P. Rayer, D. Rundle, P. Brunel, J. Vidot, P. Roquet, M. Matricardi, A. Geer, N. Bormann, and C. Lupu (2018). "An update on the RTTOV fast radiative transfer model (currently at version 12)". In: *Geoscientific Model Development* 11.7, pp. 2717–2737. DOI: 10.5194/gmd-11-2717-2018.

Shell, K. M., J. T. Kiehl, and C. A. Shields (2008). "Using the Radiative Kernel Technique to Calculate Climate Feedbacks in NCAR's Community Atmospheric Model". In: *Journal of Climate* 21.10, pp. 2269–2282. DOI: 10.1175/2007JCLI2044.1.

Sherwood, S. C., M. J. Webb, J. D. Annan, K. C. Armour, P. M. Forster, J. C. Hargreaves, G. Hegerl, S. A. Klein, K. D. Marvel, E. J. Rohling, M. Watanabe, T. Andrews, P. Braconnot, C. S. Bretherton, G. L. Foster, Z. Hausfather, A. S. von der Heydt, R. Knutti, T. Mauritsen, J. R. Norris, C. Proistosescu, M. Rugenstein, G. A. Schmidt, K. B. Tokarska, and M. D. Zelinka (2020). "An Assessment of Earth's Climate Sensitivity Using Multiple Lines of Evidence". In: *Reviews of Geophysics* 58.4, e2019RG000678. DOI: 10.1029/2019RG000678.

Sherwood, S. C., W. Ingram, Y. Tsushima, M. Satoh, M. Roberts, P. L. Vidale, and P. A. O'Gorman (2010). "Relative humidity changes in a warmer climate". In: *Journal of Geophysical Research: Atmospheres* 115.D9. DOI: 10.1029/2009JD012585.

Simpson, G. (1928a). "Some studies in terrestrial radiation." In: *Mem. R. Meteorol. Soc.* 2, pp. 69–95.

– (1928b). "Further studies in terrestrial radiation." In: *Mem. R. Meteorol. Soc.* 3, pp. 1–26.

Soden, B. J., I. M. Held, R. Colman, K. M. Shell, J. T. Kiehl, and C. A. Shields (2008). "Quantifying Climate Feedbacks Using Radiative Kernels". In: *Journal of Climate* 21.14, pp. 3504–3520. DOI: 10.1175/2007JCLI2110.1.

Soden, B., D. Jackson, V. Ramaswamy, M. Schwarzkopf, and X. Huang (2005). "The Radiative Signature of Upper Tropospheric Moistening". In: *Science (New York, N.Y.)* 310, pp. 841–4. DOI: 10.1126/science.1115602.

Suttles, J. T., R. N. Green, G. L. Smith, B. A. Wielicki, I. J. Walker, V. R. Taylor, and L. L. Stowe (1989). "Angular radiation models for Earth–atmosphere system, Vol. II — Longwave radiation". In: *NASA Tech. Rep* RP-1184.

Tung, K. K. and H. Yang (1994). "Global QBO in Circulation and Ozone. Part I: Reexamination of Observational Evidence". In: *Journal of Atmospheric Sciences* 51.19, pp. 2699–2707. DOI: 10.1175/1520-0469(1994)051<2699:GQICAO>2.0.CO;2.

Whitburn, S., L. Clarisse, S. Bauduin, M. George, D. Hurtmans, S. Safieddine, P. F. Coheur, and C. Clerbaux (2020). "Spectrally Resolved Fluxes from IASI Data: Retrieval Algorithm for Clear-Sky Measurements". In: *Journal of Climate* 33.16, pp. 6971–6988. DOI: 10.1175/JCLI-D-19-0523.1.

Williams, K. D., W. J. Ingram, and J. M. Gregory (2008). "Time Variation of Effective Climate Sensitivity in GCMs". In: *Journal of Climate* 21.19, pp. 5076–5090. DOI: 10.1175/2008JCLI2371.1.

Versicherung an Eides statt

Hiermit versichere ich an Eides statt, dass ich die vorliegende Arbeit im Studiengang M.Sc. Meteorologie selbstständig verfasst und keine anderen als die angegebenen Hilfsmittel – insbesondere keine im Quellenverzeichnis nicht benannten Internet-Quellen – benutzt habe. Alle Stellen, die wörtlich oder sinngemäß aus Veröffentlichungen entnommen wurden, sind als solche kenntlich gemacht. Ich versichere weiterhin, dass ich die Arbeit vorher nicht in einem anderen Prüfungsverfahren eingereicht habe und die eingereichte schriftliche Fassung der auf dem elektronischen Speichermedium entspricht.
Einer Veröffentlichung der vorliegenden Arbeit in der zuständigen Fachbibliothek des Fachbereichs stimme ich zu.

Hamburg, den 19.8.2021 Unterschrift: